PHYSICAL REVIEW C **111**, 034302 (2025)

Collective excitations in ^{150}Gd

S. Pascu,[1,2,*] E. Yüksel,[1] Abhishek,[1] P. Stevenson,[1] G. H. Bhat,[3] R. N. Mao,[4] K. Nomura,[5,6] C. Costache,[2]
Z. P. Li,[4] N. Mărginean,[2] C. Mihai,[2] T. Naz,[7] N. Paar,[8] Zs. Podolyák,[1] P. H. Regan,[1,9] A. E. Turturică,[2]
R. Borcea,[2] M. Boromiza,[2] D. Bucurescu,[2] S. Călinescu,[2] C. Clisu,[2] A. Coman,[2] I. Dinescu,[2] S. Doshi,[10]
D. Filipescu,[2] N. M. Florea,[2] A. Gandhi,[2] I. Gheorghe,[2] A. Ionescu,[2] R. Lică,[2] R. Mărginean,[2] R. E. Mihai,[2,11]
A. Mitu,[2] N. Nazir,[12] A. Negret,[2] C. R. Niţă,[2] E. B. O'Sullivan,[1,9] C. Petrone,[2] S. E. Poulton,[1,9]
J. A. Sheikh,[13] H. K. Singh,[2] L. Stan,[2] S. Toma,[2] G. Turturică,[2] and S. Ujeniuc[2]

[1] *School of Mathematics and Physics, University of Surrey, Guildford GU2 7XH, United Kingdom*
[2] *"Horia Hulubei" National Institute for R&D in Physics and Nuclear Engineering, R-77125 Bucharest-Magurele, Romania*
[3] *Department of Higher Education (GDC Shopian), Central University of Kashmir, Jammu and Kashmir 192 303, India*
[4] *School of Physical Science and Technology, Southwest University, Chongqing 400715, China*
[5] *Department of Physics, Hokkaido University, Sapporo 060-0810, Japan*
[6] *Nuclear Reaction Data Center, Hokkaido University, Sapporo 060-0810, Japan*
[7] *Department of Physics, SP College, Cluster University Srinagar, Srinagar 190001, India*
[8] *Department of Physics, Faculty of Science, University of Zagreb, Bijenička cesta 32, 10000 Zagreb, Croatia*
[9] *Marine, Medical and Nuclear Department, National Physical Laboratory, Teddington TW11 0LW, United Kingdom*
[10] *School of Computing Engineering and Mathematics, University of Brighton, Brighton BN2 4AT, United Kingdom*
[11] *Institute of Experimental and Applied Physics, Czech Technical University in Prague, Husova 5, Prague, Czech Republic*
[12] *Department of Physics, University of Kashmir, Hazratbal, Srinagar 190 006, India*
[13] *Department of Physics, Islamic University of Science and Technology, Jammu and Kashmir 192 122, India*

(Received 23 August 2024; accepted 23 January 2025; published 4 March 2025)

Mean lifetime measurements of low-lying yrast positive- and negative-parity states of ^{150}Gd have been performed with the ROSPHERE array using the ^{140}Ce(^{13}C,3n) fusion-evaporation reaction and the recoil distance Doppler shift method. Precise branching ratios have been obtained from a complementary electron capture decay experiment of both the isomer and ground state of ^{150}Tb. Reduced $E1$, $E2$, and $E3$ transition probabilities were extracted and compared with the corresponding observables in the neighboring isotopes and isotones. The experimental data are compared to the predictions of various theoretical models: quasiparticle random phase approximation, time-dependent Hartree-Fock calculations, the quadrupole-octupole collective Hamiltonian, the mean-field mapped interacting boson model, and the triaxial projected shell model. We find that a complete description of both quadrupole and octupole collectivity, from ground and excited states, is currently lacking, and such measurements of transition strengths are crucial for constraining present and future calculations.

DOI: 10.1103/PhysRevC.111.034302

I. INTRODUCTION

The equilibrium shape of atomic nuclei is one of the most basic properties these many-body quantum systems possess. The rare-earth region is interesting from this point of view since quadrupole [1], octupole [2], tetrahedral shapes [3], and shape coexistence [4] have been theoretically predicted and experimentally confirmed. The quadrupole-deformed nuclei in this region are traditionally interpreted as having an axially symmetric shape, and are often considered as textbook examples of prolate-deformed nuclei, as proposed by Bohr and Mottelson [1]. This picture remained unchanged for more than 70 years, until recent calculations within the Monte Carlo shell model (MCSM) highlighted the importance of the tensor force for the nuclear shapes, and proposed that in the rare-earth region, triaxially deformed nuclei are predominant rather than the prolate-deformed shapes [5,6]. This is probably one of the most significant paradigm shifts in nuclear structure in the last years, but the exact region where this occurs still needs to be constrained by experimental data.

A. Phase transition and shape competition analysis around $N \approx 90$

Phase transitions between the spherical and/or vibrational and axial-deformed regions, the so-called X(5) symmetry introduced by Iachello [7], have been proposed to occur in several $N = 90$ nuclei [8,9], including ^{154}Gd [10]. However, the usual signature of a flat potential energy surface (PES) was challenged by more recent investigations. In particular, studies

---

[*] Contact author: sorin.pascu@nipne.ro

with the constrained relativistic mean-field approach with the NL3 interaction [11] or within the Hartree-Bogoliubov model [12] found ^{150}Gd and ^{152}Gd among critical point symmetry candidates.

Indeed, even the degree of deformation of the nuclei in this region is an area of much discussion in the literature, with some theoretical studies placing ^{150}Gd in the spherical region (Nilsson model [13], consistent Q formalism (CQF), and phenomenological interacting boson model (p-IBM) [14]). On the other hand, other investigations predict a moderate deformation; these include (i) the mean-field mapped interacting boson model (m-IBM) [14]; (ii) the five-dimensional collective Hamiltonian based on the PC-PK1 covariant density functional theory (CDFT) [15]; (iii) the triaxial projected shell model (TPSM) [16]; (iv) the relativistic Hartree-Bogoliubov implementation of the covariant density functional theory [17]; (v) the constrained relativistic mean field [11]; (vi) the Skyrme Hartree-Fock + BCS model [18], albeit with a low β_2 deformation [19]; (vii) the five-dimensional collective quadrupole Hamiltonian (5DCH) [20]; (viii) the phenomenological interacting boson model [21]; and (ix) relativistic mean-field theory with the NL-SH parameter set [22]. Beyond mean-field and Gogny D1S calculations revealed that none of the calculated PESs in the Gd isotopes shows the presence of a critical point, suggesting the importance of triaxial degree of freedom in the $N = 86$–90 isotopes [23].

B. Octupole collectivity in the rare-earth region

Octupole correlations are known to play an important role around the $N \approx 88$ isotonic chain [24]. The emergence of octupolarity is understood as being due to the presence in this region of single-particle orbitals with $\Delta l = \Delta j = 3$. Close to magic nuclei, octupole collectivity is the consequence of several such orbital pairs across the neutron and proton shell gaps. In quadrupole-deformed nuclei, the octupole collectivity is related to such orbital pairs within a single shell. In the rare-earth region, the coupling between the $h_{11/2}$ ($i_{13/2}$) and $d_{5/2}$ ($f_{7/2}$) proton (neutron) single-particle orbitals is the main reason for the increased octupole correlations. The largest electric octupole ($E3$) transitions in this region, to date, have been measured in ^{144}Ba (48^{+25}_{-34} W.u.) [2] and ^{146}Ba (48^{+21}_{-29} W.u.) [25]. In addition, enhanced octupole correlations have been claimed in ^{144}Ce [26], ^{150}Nd [27], and ^{148,150,152}Sm, [28], but mostly inferred from the behavior of the $E1$ decay strength. Nevertheless, the enhanced octupole collectivity in the rare-earth region appears to be of vibrational nature, as compared to the situation in the actinides, which is the only known region so far that shows examples of octupole deformation [27,29]. Finally, we emphasize an interesting result in the case of ^{152}Sm, where a pattern of repeating excitations of negative parity has been found built on the 0^+_2 state. These are similar to the one built on the ground state and support the idea of shape coexistence rather than a distinct critical-point-related phase change [30].

Experimental signatures for increased octupole correlations in even-even nuclei include the presence of alternating bands and enhanced $E3$ transition strengths. In ^{146}Gd ($N = 82$), the first excited level is a $J^\pi = 3^-$ state, which decays directly to the ground state via a collective $E3$ transition with $B(E3) = 37(4)$ W.u. [31]. An even larger $E3$ strength of 41(6) W.u. was measured in ^{148}Gd ($N = 84$) [32], suggesting that the $f_{7/2}$-$i_{13/2}$ neutron orbital pair starts to contribute. In ^{150}Gd ($N = 86$), alternating-parity bands start from the $J^\pi = 3^-$ excitation energy [33], which is notably lower than in the neighboring isotopes. In addition, we have recently reported a very large $B(E3)$ value in ^{150}Gd [34] (45(5) W.u.), continuing the increasing trend of octupole collectivity in the Gd nuclei. However, for ^{152}Gd, no $E3$ strength has been reported so far, while for the heavier Gd isotopes, the octupole strength lies around 15–20 W.u. [35].

Calculations with the mean-field constrained interacting boson model for the Sm and Gd isotopes [36] predict a small β_3 value for the $N = 86$ and $N = 88$ isotones in the mean-field calculations, but a vanishing value when projecting into the IBM model space. Moreover, the $E3$ strength across the whole Gd isotopic chain shows only small variations with neutron number, in contrast with the experimental situation. More pronounced octupole minima are found in the previous relativistic mean-field calculations, with a value of $\beta_3 = 0.08$ for ^{148}Sm [37]. However, no $E3$ strength was extracted from those calculations. A systematic study to search for octupole-deformed nuclei has been performed with the Skyrme-Hartree-Fock + BCS model, and the results support the presence of a small octupole minimum with a value of 0.06 in the case of ^{150}Gd [18]. The results of the calculations with the quadrupole-octupole collective Hamiltonian in Ref. [38] found no stable minima for any Gd isotope. Hartree-Fock-Bogoliubov calculations using the Gogny energy density functional (EDF) with D1M and D1S parametrizations have found ^{150}Gd to lie at the border of the shape transition from octupole- to quadrupole-deformed ground states [39]. The collective model of coherent quadrupole and octupole motion (CQOM) was applied in Ref. [40] to heavier Gd isotopes ($A = 154$–158) and gives a qualitative description of $B(E3)$ transition probabilities. Finally, we mention two studies performed for the $N = 86$ isotones. The first one is experimental, and extracted the dipole moments from $B(E1)/B(E2)$ probabilities [41]. The results indicate a reduction of the dipole moments starting with $Z > 62$. The second one concerns the theoretical calculations within the adiabatic time-dependent Hartree-Fock plus zero point energy in the cranking approximation. The results indicate relatively shallow octupole barriers and give a reasonable description of the experimental data [42].

C. Present experimental status and current work

^{150}Gd is a nucleus located two neutrons away from the stability line, and has been previously studied using a variety of reactions, including α- and β-decay studies, transfer reactions, as well as light- and heavy-ion fusion evaporation reactions [33]. However, only a handful of mean lifetimes of low-lying excited states have been reported so far [34,43]. Results concerning the mean lifetime determination of the 3^- and 5^- states, and of the corresponding branching ratios, have already been published [34]. In the current work, we present complete results of our study for mean lifetime measurements in ^{150}Gd. In addition, we present partial results from a complementary electron capture (EC) decay experiment used to extract γ-ray branching ratios needed to calculate the final electromagnetic transition strengths. In Sec. II, we describe the experimental setups and the details of the two experiments. Experimental results are given in Sec. III, and compared in Sec. IV to theoretical calculations within the quasiparticle random phase approximation (QRPA), time-dependent Hartree-Fock (TDHF) calculations, the mean-field mapped interacting boson model (m-IBM), the quadrupole-octupole collective Hamiltonian (QOCH), and the TPSM.

II. EXPERIMENTAL DETAILS

A. RDDS experiment

Mean lifetime measurements were performed using the recoil distance Doppler shift method [44]. Excited states of ^{150}Gd were populated with the ^{140}Ce(^{13}C,3n) fusion-evaporation reaction with 62 MeV ^{13}C ions delivered by the Tandem accelerator of the "Horia Hulubei" National Institute for Research and Development in Physics and Nuclear Engineering (IFIN-HH) near Bucharest. The average current was kept at about 5 particle nanoamperes (pnA) throughout the experiment and impinged on a thin 0.5 mg/cm^2 ^{140}Ce layer deposited on a stretched 3 mg/cm^2 Au foil facing the beam. The stopper consisted of 4 mg/cm^2 Au, which was sufficient to stop the recoiling ions with an average velocity of $v/c = 0.70(4)\%$.

Measurements were taken over ten separate target-stopper foil distances, ranging from 20 to 500 μm to cover a broad range of lifetime sensitivity. Emitted γ rays were detected with the ROSPHERE array [43], consisting of 14 HPGe detectors and 11 LaBr$_3$(Ce) scintillators. The HPGe detectors were arranged in four rings, covering four polar angles: 37° (five), 90° (three), 110° (one), and 143° (five). The LaBr$_3$(Ce) scintillators were mounted in the remaining positions.

In the present paper, we show the results obtained with the HPGe detectors and the plunger method using the spectra collected with the detectors placed at 37° and 143°. The full-energy peak detection efficiency of the setup was about 1.1% for the HPGe array at 1332 keV [43]. The HPGe and LaBr$_3$(Ce) detectors were calibrated in energy and efficiency using a ^{152}Eu standard source. In addition, a run-by-run gain matching procedure was applied to correct for additional shifts during the experiment.

Data were analyzed using the differential decay curve method (DDCM) [45,46]. We employed the γ-γ coincidence version of this technique which is well suited for eliminating the feeding of the level, which affects single γ-ray measurement. The shifted (called "s") and unshifted (called "u") intensities of the depopulating transition (called A) are determined from the measured γ-ray intensities. In the case of direct feeding, the gate is set on the shifted component of the populating transition (called B) of the level of interest and ensures that the depopulating transition is emitted in flight. The mean lifetime τ is determined with the following equation [46]:

$$\tau_i(d) = \frac{I_{uA}^{sB}(d)}{v\frac{d}{dt}I_{sA}^{sB}(d)}, \tag{1}$$

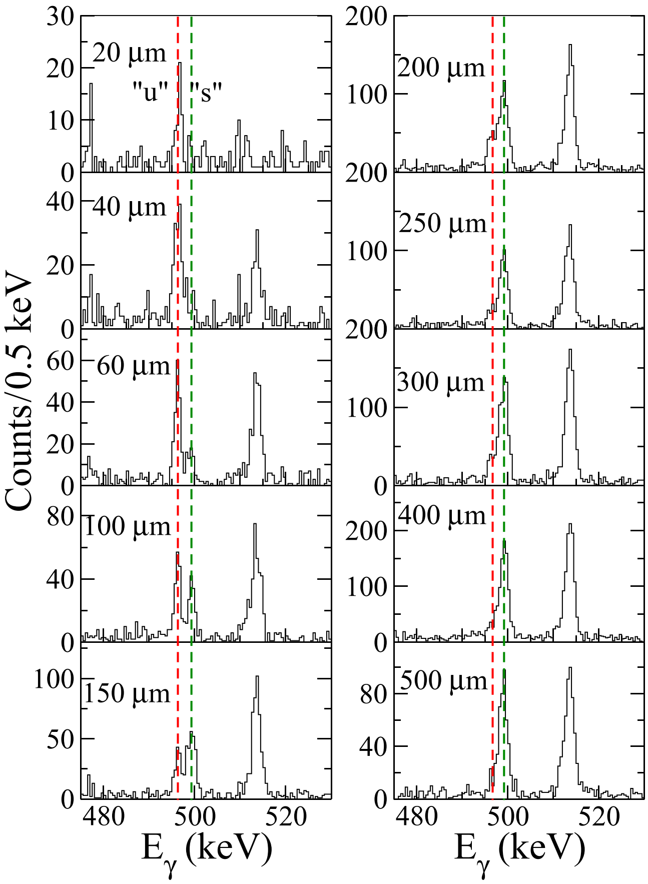

FIG. 1. Evolution of the shifted ("s", dashed green line) and unshifted ("u", dashed red line) components of the 496-keV γ line ($3^- \rightarrow 2^+$ transition), measured at 37° relative to the beam axis. Spectra were obtained by gating on the shifted component of the 566-keV transition ($5^- \rightarrow 3^-$) at 143°.

where I_{uA}^{sB} and the I_{sA}^{sB} are coincident intensities, namely, the unshifted and the shifted component of transition "A" when gated by the shifted component of transition "B", respectively. Since the denominator involves the derivative of shifted components, which is not directly measured, I_{sA}^{sB} components are fitted piecewise with easily derivable functions. In the present case, second-degree polynomials were used, and the program Napatau was employed [47]. In the case of the indirect gating, on a higher feeding transition (called "C"), the gate is set on the shifted component of the transition "C" and Eq. (1) can be rewritten as [46]

$$\tau_i(d) = \frac{I_{uA}^{sC}(d) - \alpha I_{uB}^{sC}(d)}{v\frac{d}{dt}I_{sA}^{sC}(d)}, \tag{2}$$

where α is defined as [46]

$$\alpha = \frac{I_{sA}^{sC}(d) + I_{uA}^{sC}(d)}{I_{sB}^{sC}(d) + I_{uB}^{sC}(d)}. \tag{3}$$

Sample spectra obtained from the current experiment are presented in Fig. 1. The region around 500 keV is magnified to illustrate the evolution with distance of the shifted ("s") and unshifted ("u") components of the main transition

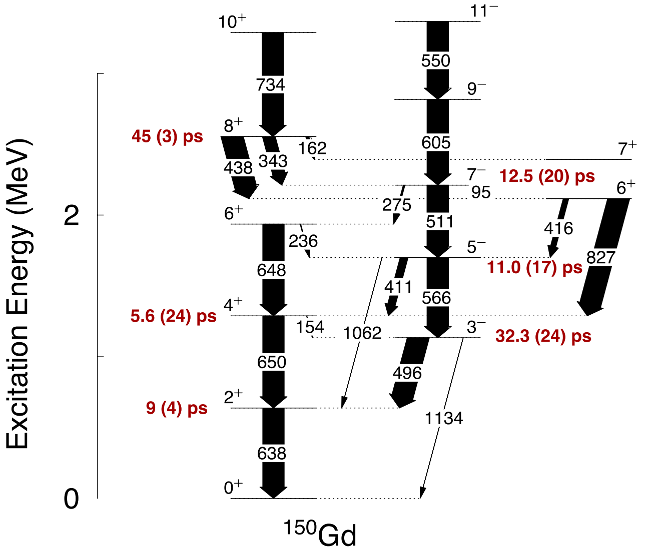

FIG. 2. Relevant part of the level scheme of ^{150}Gd showing low-lying excited states up to $J^\pi = 11^-$, with the width of the arrows proportional to the experimental intensity (see Table I for exact values). The mean lifetimes deduced from the present experiment are shown in red next to the corresponding level.

(496 keV) depopulating the first 3^- level at 1134.3 keV [33] (see Fig. 2). The spectra are gated by the shifted component of the $5^- \rightarrow 3^-$ transition (566 keV) located just above the 3^- level. The separation between the shifted and unshifted components is about 3.5 keV at this energy, which is enough to distinguish between the two peaks. To ensure a clean gate, only half of the shifted feeding peak was used as a gate, the one further apart in energy from the unshifted component (i.e., the highest energy for the forward direction and the lowest for the backward direction). The width of the gate was modified until a component of the stopped peak was clearly observed in the gated spectra (the shifted/unshifted ratio was changed because of the additional presence of a stopped component). A relevant part of the low-lying ^{150}Gd level scheme, for both the positive- and negative-parity levels up to around 3.5 MeV, is presented in Fig. 2. The mean lifetimes are indicated on the figure close to the levels they represent. The width of the arrows is proportional to the γ-ray intensities obtained from the electron capture decay experiment described in the next section. The current values are more precise, and most of them agree with the previously determined branching ratios in Ref. [33], with some discrepancies in the case of the decay of the 5^- level at 1699.9 keV (see Table I).

An important point in the DDCM analysis is the normalization of data for different distances. One of the possible normalizations is to the total number of events in each angle-gated γ-ray energy coincidence matrix. This number is usually proportional to the time data were collected for each distance and the beam intensity during that period. However, in the present experiment, the target material was deposited on an Au backing. At 62 MeV, the ^{13}C beam induced another reaction on the backing, producing mostly ^{206}At, which decays back to ^{206}Po with a half-life of $T_{1/2} = 30.6(8)$ min [49]. The decay chain continues down to ^{206}Pb, with half-lives of several days ($T_{1/2}(^{206}\mathrm{Po}) = 8.8(1)$ days and $T_{1/2}(^{206}\mathrm{Bi}) = 6.243(3)$ days [49]). As such, the total number of counts in the spectrum slightly increases over time as the target is activated

TABLE I. Summary of relevant experimental results for ^{150}Gd. The state energy (E_i), the mean lifetime (τ), the initial (J_i^π) and final spin and parity (J_f^π), the energy of the final state (E_f), the decay transition (E_γ), the multipolarity (Mult.), the branching ratios from the present experiment (normalized to the most intense γ ray for each level) (I_γ expt.) and the corresponding literature values (I_γ lit.), the conversion coefficient α_{ICC} calculated with the bricc code [48], and the corresponding transition probabilities are listed. The multipolarity of the 1061-keV transition (in square brackets) is not given in Ref. [33] and is assumed in the present measurement as having an $E3$ character based on spin difference.

E_i (keV) [33]	τ (ps)	J_i^π [33]	J_f^π [33]	E_f (keV) [33]	E_γ (keV) [33]	Mult. [33]	I$_\gamma$ expt.	I$_\gamma$ lit. [33]	α_{ICC} [48]	$B(E\lambda)\downarrow$ (W.u.)
638.045(14)	9(4)	2_1^+	0_1^+	0.0	638.050(16)	$E2$	100	100	0.00754	19_{-7}^{+16}
1134.297(17)	32.3(24)	3_1^-	2_1^+	638.045(16)	496.242(15)	$E1$	100(2)	100	0.00479	$8.7(7) \times 10^{-5}$
			0_1^+	0.0	1134.1(1)	$E3$[a]	0.27(2)		0.00439	45(5)
1288.42(3)	5.6(24)	4_1^+	3_1^-	1134.297(17)	154.07(6)	$(E1)$	1.5(1)	1.8(4)	0.0911	$2.5_{-8}^{+18} \times 10^{-4}$
			2_1^+	638.045(16)	650.36	$E2$	100(2)	100	0.00720	26_{-8}^{+19}
1699.912(25)	11.0(17)	5_1^-	4_1^+	1288.42(3)	411.490(15)	$E1$	46(1)	77(4)	0.00738	$1.4_{-2}^{+3} \times 10^{-4}$
			3_1^-	1134.297(17)	565.64(2)	$E2$	100(2)	100	0.01015	18(3)
			2_1^+	638.045(16)	1061.5(1)	$[E3]$[b]	0.10(2)		0.00513	53_{-12}^{+15}
2211.11(14)	12.5(20)	7_1^-	6_2^+	2115.75(9)	95.5(2)	$(E1)$	1.3(1)	2.0(4)	0.331	$3.8_{-6}^{+8} \times 10^{-4}$
			6_1^+	1936.31(16)	274.9(3)	$E1$	6.1(1)	8(3)	0.0199	$7.4_{-10}^{+14} \times 10^{-5}$
			5_1^-	1699.912(25)	511	$E2$	100(2)	100(16)	0.01318	36_{-5}^{+7}
2554.14(12)	45(3)	8_1^+	$(7)_1^+$	2392.06(17)	162.0(2)	$M1$	14(2)	14(4)	0.513	0.0125(18)
			7_1^-	2211.11(14)	343.07(10)	$E1$	62(5)	59(19)	0.01142	$6.3(6) \times 10^{-5}$
			6_2^+	2115.75(9)	438.37(10)	$E2$	100(2)	100(45)	0.0199	12.8(10)

[a] From current work.

[b] Assumed in the present measurement based on spin difference.

and decays toward stability. Therefore, the present experiment used a normalization to the main Au lines Coulomb excited in the reaction, for each angle-gated γ-ray energy coincidence matrix.

The mean lifetimes determined in the present experiment are summarized in Table I, together with their initial and final states and spin values, the decay transition energy and multipolarity, the deduced intensity in the present experiment in comparison with the literature values, the internal conversion coefficient, and the transition strengths. The mean lifetimes were calculated as a weighted average of all possible ring-ring combinations where they could be determined without interference from contaminating peaks. A systematic uncertainty of 5% is added in quadrature to the quoted mean lifetimes to account for the uncertainty in the velocity distribution, except for the mean lifetime of the 7^-_1 level at 2211.1 keV for which an additional 5% is added to account for the presence of possible random coincidences, as discussed below.

B. Electron capture decay experiment

A precise measurement of the branching ratios necessary to extract the reduced transition strengths was performed following an electron capture decay measurement of ^{150}Tb. The parent nucleus was produced in the ^{147}Sm(^{6}Li,3n) fusion-evaporation reaction with an incident energy of 33 MeV impinged on a 9.4 mg/cm^2 ^{147}Sm target enriched to 94% ($Q_{\mathrm{EC}} = 4.7$ MeV). ^{150}Tb has a $J^\pi = (2)^-$, $T_{1/2} = 3.48(16)$ h [33] ground state and will mainly populate low-spin states having a spin of $J = 1, 2, 3$, and a $J^\pi = 9^+$, $T_{1/2} = 5.8(2)$ min [33] isomer populating mostly high-spin states with $J = 8, 9, 10$. The large time difference between these two competing EC decay branches from ^{150}Tb makes it easier to disentangle them and to measure clean decay spectra arising primarily from the ground-state decay branch. Therefore, two beam-on and beam-off settings were used to separate them. To enhance the isomer production, a 10 min/10 min beam-on/beam-off period was used, while for the ground-state decay, we used a 5-h activation period, followed by 1 h of cooling without data taking, and 5 h of ground-state decay measurement. Data were collected with the ROSPHERE array in a configuration with 21 HPGe detectors placed at 37° (five), 70° (five), 90° (one), 110° (five), and 143° (five). The detectors were calibrated with ^{152}Eu and ^{56}Co standard radioactive sources, followed by a gain matching for each run. In the present paper, we only show the results from the decay of the high-spin isomer necessary to complement the plunger data and extract the transition strengths. A detailed analysis of both the isomer and ground-state decay of ^{150}Tb will be given elsewhere [50].

III. RESULTS OF THE ANALYSIS

A. Mean lifetimes of the positive-parity states

The mean lifetimes of three positive-parity states were measured in this experiment: the 2^+_1 at 638 keV, the 4^+_1 at 1288 keV, and the 8^+_1 at 2554 keV. The lifetime of the first 2^+ level was determined from an indirect gating on the 566 keV $5^- \rightarrow 3^-$ transition. This was the only viable gate that could be used in the present study and offered sufficient statistics. A clean direct gating on the $4^+ \rightarrow 2^+$ 650-keV transition is not possible because of the presence of the $6^+ \rightarrow 4^+$ 648-keV γ ray, with a difference of only 2 keV (see Fig. 2). A possible solution can be a gate on the 496-keV $3^- \rightarrow 2^+$ transition. However, the mean lifetime of the intermediate 3^- state is longer than that of the 2^+ level, so the unshifted component of this transition is extremely small in the region of sensitivity of the 2^+ state. As a result, the mean lifetime of this level is determined with a large uncertainty (see Table I). The mean lifetime and the evolution of the shifted and unshifted components corresponding to the 2^+ state are shown in Figs. 3(a) and 3(d) in the case of a forward-backward matrix.

The mean lifetime determination of the first 4^+ level (1288 keV) suffers from the same lack of a clean gate because of the contaminating $6^+ \rightarrow 4^+\gamma$ transition. Therefore, the lifetime was determined from a direct gate on the 411-keV $5^- \rightarrow 4^+$ transition. However, due to the low statistics, clear shifted and unshifted components of the 650-keV transition are visible at only three angles, resulting in about 40% uncertainty (see Table I). The extracted mean lifetime and the evolution of the shifted and unshifted components corresponding to the 4^+ state are shown in Figs. 3(b) and 3(e) in the case of a forward-backward matrix.

The 8^+ level at 2554 keV is the lowest energy state with this spin and, therefore, can be considered a part of the yrast band. However, a careful examination of its decay pattern reveals a dominant decay to a second 6^+ state at 2116 keV. In fact, no direct transition to the 6^+_1 state has been observed so far [33]. This suggests that the structure of the first 8^+ state is vastly different from the lower-spin states (2^+ to 6^+). A strong transition above the 8^+ level is seen (734-keV line depopulating the 10^+ state at 3288 keV. Therefore, the lifetime of this state is determined with below 10% uncertainty. Figs. 3(c) and 3(f) show the lifetime of the 8^+ level and the evolution of the shifted and unshifted components of the 438-keV transition.

B. Mean lifetimes of the negative-parity states

In the present experiment, we deduced the mean lifetimes of three negative-parity states: 3^-_1 at 1134 keV, 5^-_1 at 1700 keV, and 7^-_1 at 2211 keV. All the values in the present section are determined using Eq. (1) from direct gating. The three levels of interest are all part of the octupole band, so the determination of their mean lifetimes is essential for the discussion in the following section. The values for the 3^-_1 and 5^-_1 states have been reported previously in Ref. [34], so in the following, we only review these results.

The mean lifetime of the 3^-_1 level is determined from a gate on the 566-keV $5^- \rightarrow 3^-$ direct feeder and is presented in Fig. 4(a), while the evolution of the shifted and unshifted components of the 496-keV transition is shown in Fig. 4(d). Since the mean lifetime of the 3^-_1 level is relatively long compared to the other low-lying states in this nucleus, the shifted and unshifted components are seen at seven distances. As a result, a precise measurement with an uncertainty below 10% could be performed.

The mean lifetime of the 5^-_1 level at 1700 keV was determined from direct gating on the shifted component of the $7^- \rightarrow 5^-$ 511-keV transition. The evolution of the shifted and

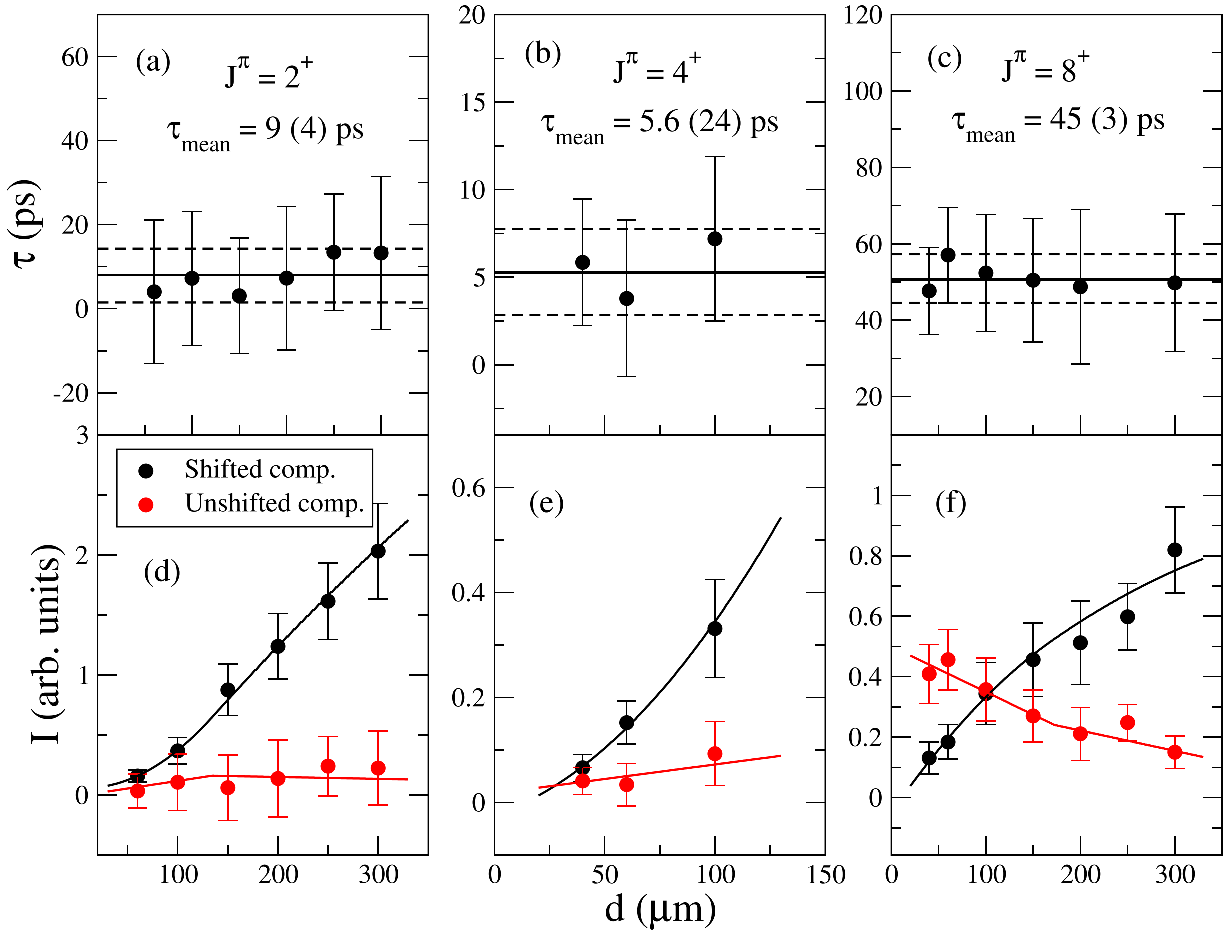

FIG. 3. Top: Mean lifetimes of the low-lying positive-parity states (first 2^+, 4^+, and 8^+) of ^{150}Gd as a function of plunger distance. 1σ uncertainties are given as dashed lines. Bottom: Relative intensities of the shifted and unshifted components and their corresponding fit with second-degree polynomials for a forward-backward matrix (see text for details).

unshifted $5^- \to 3^-$ 566-keV γ-ray components was followed for all distances in the sensitivity region (five distances) and is presented in Fig. 4(e).

The 7_1^- level at 2211 keV decays mainly by a 511-keV γ ray to the 5_1^- state. The other two decay transitions, located at 95 keV ($I_\gamma = 1.3(1)\%$) and 275 keV ($I_\gamma = 6.1(1)\%$) (see Table I and the following section), are located at lower energies (their shifted and unshifted components cannot be separated with the present energy resolution of the detectors) and are too weak to show any significant statistics. Therefore, the mean lifetime determination of the 7_1^- level has to rely on the 511-keV transition. Of course, the well-known annihilation line has, unfortunately, exactly the same energy and will contribute to the present spectra in the stopped component of the $7^- \to 5^-$ transition. Although this will be much reduced for coincident events, we cannot exclude the contribution of this component through random coincidences. Therefore, gated spectra on transitions that are not in "true" coincidence with the $7^- \to 5^-$ transition were inspected. The forward-backward matrix at 20 μm was chosen and the obtained spectra are presented in Fig. 5, with a gate on the 438-keV $8_1^+ \to 6_2^+$ transition in Fig. 5(a), and a gate on the 827-keV $6_2^+ \to 4_1^+$ transition in Fig. 5(b). The main transitions are indicated in the figure, while it can clearly be seen that there is hardly any contribution of the 511-keV line in the spectra (dashed line indicates the location of the supposed 511-keV γ ray). Nevertheless, we decided to add an additional 5% systematic uncertainty to our determined lifetime to account for this possible contamination. The results are presented in Figs. 4(c) and 4(f).

We note that the full horizontal lines in Figs. 3(d)–3(f) and 4(d)–4(f) represent the values extracted only from the forward-backward combination of detectors as explained above, while the mean lifetime indicated on each panel is the weighted average value extracted from all possible detector combinations.

C. Determination of the branching ratios

Branching ratios were determined using the γ-γ coincidence data from the EC decay experiment. All the results presented in Table I are obtained by "gating from above." This method implies placing a gate on a transition above the one of interest and dividing the intensity of the γ ray of interest by the intensity of the strongest transition out of that level, corrected by efficiency. To check the accuracy of the

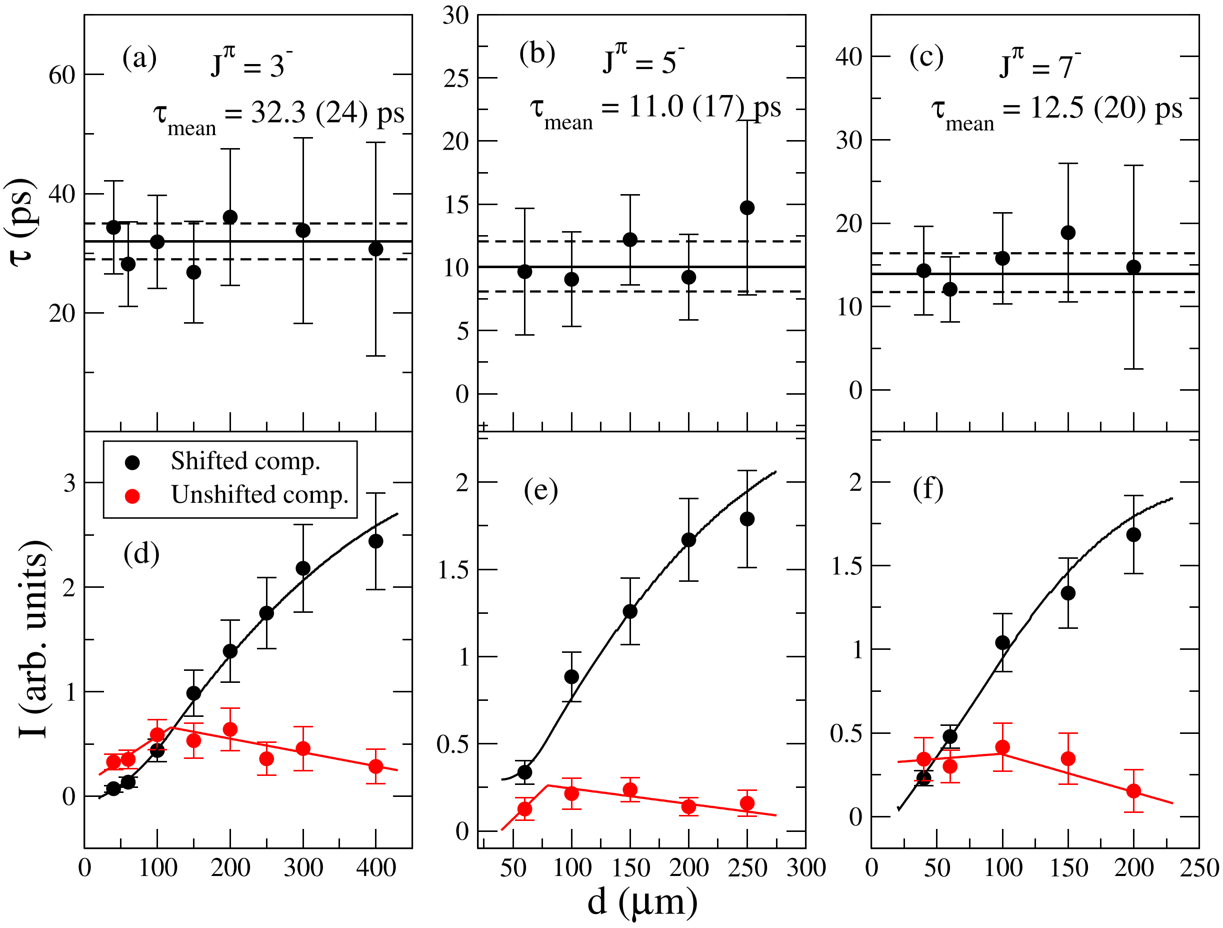

FIG. 4. Similar to Fig. 3, but for the 3_1^-, 5_1^-, and 7_1^- negative-parity states.

results, the "gating from below" method was also employed, as described in Ref. [51]. Angular correlation effects were neglected in the present analysis.

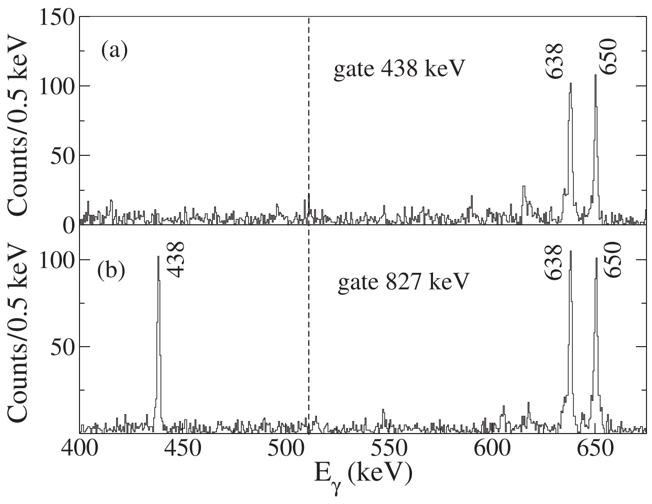

FIG. 5. Relevant part of the γ-ray spectrum gated by (a) the 438-keV transition and (b) the 827 keV transition). The main γ lines in the spectra are indicated. The dashed line corresponds to the position of the 511-keV transition from random coincidences.

The $3^- \rightarrow 0^+$ transition was observed in the EC decay experiment and reported for the first time in Ref. [34]. Since only limited information could be given in that paper, we present below a complete description of the determination of this branching ratio.

A gated spectrum on the 566-keV transition ($5^- \rightarrow 3^-$) is presented in Fig. 6(a). A clear 1134-keV peak can be seen. This corresponds to the $3^- \rightarrow 0^+$ transition, as well as to the case when the two individual γ rays at 638 and 496 keV, corresponding to $2^+ \rightarrow 0^+$ and $3^- \rightarrow 2^+$, are detected in the same detector in the same time window. This process is called summation and has to be subtracted in order to obtain the "true" intensity of the $3^- \rightarrow 0^+$ transition. To estimate the level of summation, we rely on the summation observed between transitions 638 and 566 keV, gated on the 496-keV line. The summation peak is shown in Fig. 6(b) and has an energy of 1204 keV. In addition, we also estimated the branching ratio from gating on the 343-keV transition ($8^+ \rightarrow 7^-$), as well as on the 566-, 343-, and 511-keV lines on a γ-γ-γ matrix, and looking for the summation of the $3^- \rightarrow 2^+$ and $2^+ \rightarrow 0^+$ transitions. The branching ratio is taken as a weighted average of all these cases. Another "contamination" source of the 1134-keV transition is the presence of a so-far-unobserved transition at 1132 keV. This is shown in Fig. 6(c) in the gated spectrum on 650- and 648-keV lines. Based on the γ-γ-γ coincidence data analysis, we propose the existence of a new

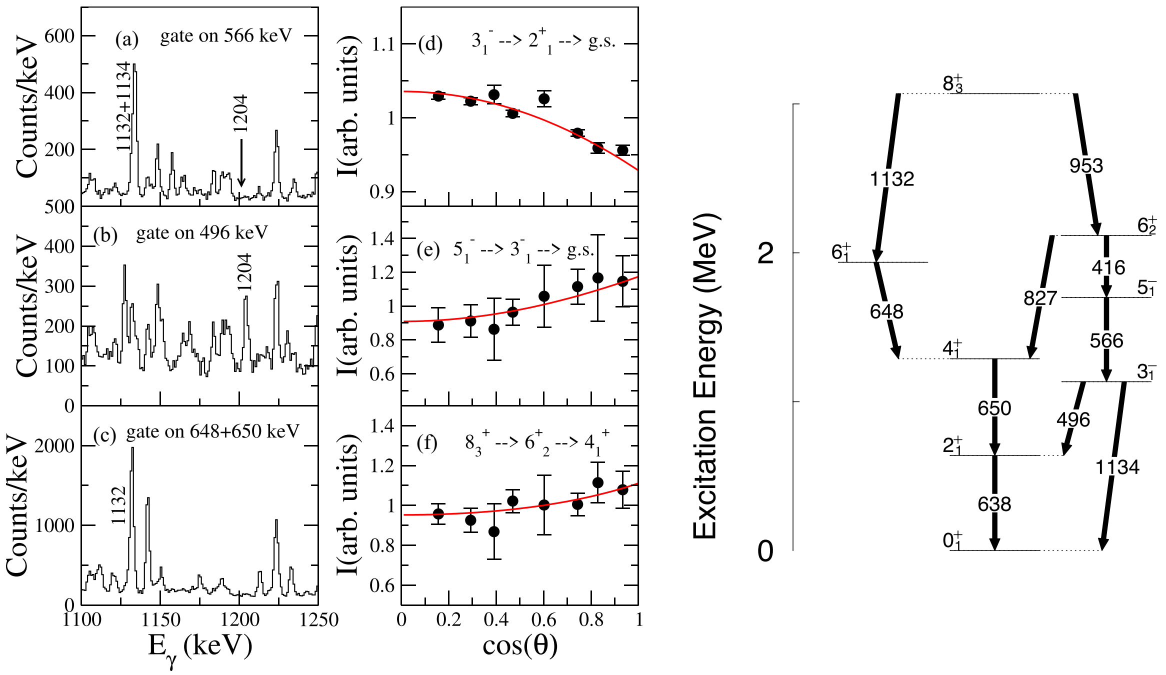

FIG. 6. EC decay experimental data. Left: (a) Part of the γ spectrum of ^{150}Gd in coincidence with 566-keV ($5^- \to 3^-$) transition showing the region around the 1134-keV ($3^- \to 0^+$) γ line. (b) Part of the γ spectrum gated on the 496-keV ($3^- \to 2_1^+$) transition showing the region around the summation peak (1204 keV) corresponding to the $5^- \to 3^-$ and $2^+ \to 0^+$ γ rays. Note that this peak is absent in panel (a), the location being indicated by an arrow. (c) Gated spectrum on the $4^+ \to 2^+$ and $6^+ \to 4^+$ transitions showing the new 1132-keV line. (d) $3_1^- \to 2_1^+ \to 0_1^+$ experimental (black points) and theoretical (red line) angular correlation assuming pure $E1$ and $E2$ multipolarities. (e) $5_1^- \to 3_1^- \to 0_1^+$ experimental (black points) and theoretical (red line) angular correlation for $E2$ and $E3$ multipolarities, respectively. (f) $8_3^+ \to 6_2^+ \to 4_1^+$ experimental (black points) and theoretical (red line) angular correlation for the newly determined state at 3069 keV ($E2$ multipolarities assumed). Angular correlations are normalized to the $6_2^+ \to 4_1^+ \to 2_1^+$ cascade. Right: Partial level scheme relevant for the determination of the previously unreported state $J^\pi = 8^+$ at 3069 keV.

level with an energy of 3069 keV, decaying with the 1132-keV transition on the 6_1^+ level at 1936 keV, and with an energy of 953 keV on the 6_2^+ level at 2116 keV (see the right part of Fig. 6 for a partial level scheme).

In addition to the statistical uncertainty, a systematic uncertainty derived from the efficiency curve and angular correlation effect was considered. We estimate that the efficiency curve introduces a 2% systematic uncertainty, while the systematic uncertainty from the angular correlations is calculated to be less than 1%. These effects are important for the determination of the $3^- \to 0^+$ transition, as explained in Ref. [34]. By adding all these contributions we obtain an intensity of 0.27(2)% relative to the 496-keV transition.

We performed angular correlation calculations to verify that the observed transition at 1134 keV corresponds to the decay of the 3_1^- level. HPGe detectors were arranged in eight groups according to their relative angle, and γ-γ matrices were created for each group. The angular correlation was normalized to the $6_2^+ \to 4_1^+ \to 2_1^+$ cascade. To verify the normalization, the $3_1^- \to 2_1^+ \to 0_1^+$ angular correlation is calculated and shown in Fig. 6(d). Figure 6(e) presents the results for the $5_1^- \to 3_1^- \to 0_1^+$ angular correlation. The experimental data are consistent with a 5-3-0 cascade (solid lines are the theoretical angular correlation curves for pure multipolarities, supporting the spin assignments). Finally, in Fig. 6(f), we show the 953–827-keV angular correlation corresponding to the decay of the newly observed state at 3069 keV. As this level is populated in the EC decay of the 9^+ isomer, the most probable spin range is $J = 8, 9, 10$. Since this level decays to the first two 6^+ states, we propose that this state has a $J = 8$ spin. The angular correlation presented in Fig. 6(f) is consistent with a $J = 8$ assignment. On the right-hand side of Fig. 6, we present the relevant level scheme for the decay of the 3069-keV level.

The results for the intensities of the transitions depopulating the low-lying states of ^{150}Gd agree in general well with the ones in the literature [33] and are more precise. The only significant difference occurs for the transitions decaying out of the 5_1^- level at 1699.9 keV. The adopted values for the mass chain $A = 150$ [33] lists three γ rays with energies 411, 566, and 1061 keV, with normalized intensities of 77(4), 100, and 15(3), respectively. In the present experiment, the three transitions depopulating the 5_1^- level have intensities of 46(1), 100(1), and 0.10(2), respectively. The largest difference appears for the 1061-keV transition, with a factor of 150 smaller in the present study. Considering the mean lifetime measured in the present study and the intensity given in Ref. [33], the transition strength would result in a $B(E3; 5_1^- \to 2_1^+)$ larger than 6100 W.u., far exceeding the recommended upper limits with a value of 100 for this mass region. With our new branching ratio, we obtain a value of 53^{+15}_{-12} W.u. The origin of this γ ray in the ENSDF file is claimed to come from two proceedings papers [52,53], which report on the properties of the high-spin structure of ^{150}Gd with the ^{124}Sn(^{30}Si, $4n\gamma$) reaction. However, no γ ray of 1061 keV was reported in these two publications. The transition was reported in the previous ϵ-decay study of ^{150}Tb [54], but only from γ-ray singles measurements. We trace back the origin of this transition to the $A = 150$ mass chain evaluation published in 1995 [55] and note that the evaluation done in 1986 [56] did not list this γ ray. The two transitions depopulating the 5^-_1 state were 412 and 567 keV with intensities of 50 and 100, respectively, and are closer to what we observe in the present measurement. We conclude that the intensity of the 1061-keV γ ray was overestimated in the singles experiment, based on the huge $B(E3)$ value that would result from our measured lifetime. Therefore, the new γ-ray intensities of this study are used to deduce the corresponding transition strengths and are given in Table I.

IV. DISCUSSION

In the current work, the structure of the Gd isotopes is interpreted via the framework of the (i) quasiparticle random phase approximation, (ii) time-dependent Hartree-Fock calculations, (iii) quadrupole-octupole collective Hamiltonian, (iv) the mean-field mapped IBM, and (v) the triaxial projected shell model. In addition to these five models, a literature survey was performed for all available theoretical predictions in this region, for Gd isotopes and for $N = 86$ isotones. In the following, we present first a brief description of the theoretical models, and then we compare the calculations for the energies and transition strengths to the corresponding experimental data.

A. Theoretical models

1. Quasiparticle random phase approximation and Time-dependent Hartree-Fock model

Collective excitations in atomic nuclei are well described by the random phase approximation (RPA) or, in the case of open-shell nuclei, by the quasiparticle random phase approximation (QRPA). The QRPA is a well-known tool discussed in many textbooks and studies; therefore, we will not delve into its details here and instead refer the reader to Refs. [57–61]. In this work, we perform calculations to study the low-lying states of ^{146,148,150}Gd using nuclear EDFs based on relativistic and nonrelativistic frameworks, assuming spherical symmetry. It should be noted that the low-lying excitations are quite sensitive to the details of the levels near the Fermi surface and thus to the interaction used in the calculations. First, we use Hartree-Fock Bardeen-Cooper-Schrieffer (HF-BCS) plus QRPA [60] with the nonrelativistic Skyrme-type SkX interaction [62] in the calculations. The SkX interaction provides low-lying states that are in good agreement with experimental data. We also perform calculations by employing the relativistic Hartree-Bogoliubov (RHB) plus relativistic quasiparticle random phase approximation (RQRPA) (see Refs. [58,59] for more information). The relativistic point-coupling interaction, denoted as DD-PCX, is used in the calculations. It was optimized not only using the ground-state properties but also the excitation properties of nuclei, including the dipole polarizability in ^{208}Pb [63].

For the TDHF calculations [64,65], we used the symmetry-unrestricted sky3d code [66], which represents wave functions in a coordinate space basis. The nonrelativistic Skyrme-type SkM* interaction [67] was employed in the calculations. Low-lying octupole states were obtained by exciting the ground state with an r^3Y_{30} octupole boost, yielding the time-dependent nuclear density and expectation value of the r^3Y_{30} operator. A Fourier transform of the time-dependent response provides the strength functions in the energy domain [68]. The $B(E3)$ values are determined by fitting a Lorentzian to the lowest peak in the octupole strength function.

2. Quadrupole-octupole collective Hamiltonian

Low-energy spectra and transition rates for both positive- and negative-parity states of nuclei are calculated using the microscopic quadrupole-octupole collective Hamiltonian [38]. The collective Hamiltonian is expressed as the sum of vibrational kinetic energy, rotational kinetic energy, and the collective potential, which depends on five collective parameters: the moments of inertia, the collective mass, and the collective potential. These terms are functions of the quadrupole and octupole deformations, β_2 and β_3, which are calculated self-consistently using the constrained RHB method [69] and are then employed in the calculation of low-energy spectra and transition rates of the nucleus. It should be noted that the current version of the model is restricted to axially symmetric shapes. More details about the theoretical framework used in the present calculations are given in Ref. [38]. In this work, we focus on the Gd isotopic chain, with detailed results presented for ^{150}Gd.

3. Mean-field constrained interacting boson model

The interacting boson model (IBM) calculations give a phenomenological description of the atomic nuclei based on the premise that the main degrees of freedom can be described by coupling pairs of fermions and treating them mathematically as bosons [70]. However, the model introduces several parameters in the Hamiltonian and transition operators that must be fitted to experimental data. Although the model has proven useful in describing the low-lying structure of many even-even nuclei (see Refs. [71–76] for selected results), the existence of free parameters in the operators makes it less reliable when extrapolating to regions with no experimental data.

To address this, a new approach introduced in Ref. [77] combines IBM with Hartree-Fock-Bogoliubov (HFB) calculations based on the Gogny EDF [78], which yields a mean-field PES without experimental input. The IBM parameters are then determined by matching the bosonic PES to the HFB PES. This is achieved using s, d, and f bosons in the model. General results for Sm and Gd are presented in Ref. [36], and the reader is referred to this paper for more details. This paper focuses on the description of the Gd isotopes, particularly ^{150}Gd.

4. Triaxial projected shell model

The projected shell model (PSM) is a semimicroscopic approach suited for studying the structure of medium- and heavy-mass deformed nuclei [79]. Compared to the conventional spherical shell model, the PSM uses a deformed basis obtained by solving the Nilsson potential [80–82]. In the case of transitional nuclei, it has been shown that the assumption of axial symmetry is no longer valid, and the triaxial degree of freedom must be introduced to account for the observed properties of these nuclei [83]. The triaxial version of the model, known as the triaxial projected shell model, has been successfully applied to a wide range of nuclei, including Ge, Ce, and Nd [84,85], Er isotopes [86], and Hf, Hg, and U nuclei [84]. Gd isotopes have recently been calculated using the TPSM approach in Ref. [16]. In this paper, we present updated and detailed calculations for ^{150}Gd.

B. Results of the calculations

1. Excitation energies

In this section, a systematic investigation of the excitation energies in the yrast band of Gd isotopes ($Z = 64$) and $N = 86$ isotones is carried out. In Fig. 7, systematics of the available experimental data for positive- and negative-parity states up to 10^+ and 9^-, respectively, are presented in comparison to the available theoretical calculations in the literature. The experimental data are represented by solid black points and are taken from the adopted levels of ENSDF for mass chains $A = 148$–160 [33,87–91]. Theoretical calculations are represented by solid lines, with the exception of TPSM, for which only calculations for ^{150}Gd were performed, and are represented by dark green triangles. Theoretical results are taken from the present calculations or from previously published papers after a thorough scan of the literature: QRPA (orange), RQRPA (violet, only the 3^- states), TDHF (cyan), QOCH (red) [38], m-IBM (light green) [36], CQOM) (blue) [40], interacting boson model calculations with s and d bosons following a general fit of the available experimental data at that time (IBM-sd, yellow) [92], the five-dimensional collective Hamiltonian based on the covariant energy density functional theory (5DCH-CDFT, brown) [15], the generator coordinate method mapped onto a five-dimensional collective Hamiltonian (5DCH, grey) [20], different versions of the coherent state model (CSM, violet, only positive parity states; CSM2, dark green dash-dotted line; GCSM, magenta) [93], and within the cranked Hartree-Fock-Bogoliubov (CHFB, black) approach [94]. Theoretical values plotted for IBM-sd [92], 5DCH-CDFT [15], and 5DCH-GCM [20] were digitized from the figures presented in these references, as no explicit values were presented. The data were extracted with the online tool from [95].

Positive-parity states in the Gd isotopes are presented in the left panels of Fig. 7. There is, in general, a good agreement between the experimental data and the calculations for all the positive-parity states up to 10^+. For the positive-parity bands, the excitation energies decrease rapidly up to $N \approx 90$ and then vary slowly with the addition of more neutrons. This is consistent with the evolution of the average quadrupole deformation. The QOCH model gives a fair reproduction of the data, especially for neutron numbers $N > 90$, but fails to reproduce the absolute excitation energy of the levels for the lighter isotopes. A difference of about 400 keV is found for the 2^+ state, with values overestimating the experimental data for ^{148}Gd ($N = 84$) and underestimating them for ^{150}Gd ($N = 86$) and ^{152}Gd ($N = 88$). One of the reasons is that the present implementation of the QOCH model includes only quadrupole and octupole degrees of freedom with the additional constraint of axial symmetry. It does not take into account other, in some cases important, degrees of freedom, such as the two-quasiparticle configurations and triaxial deformations. Out of the models we used in the present paper, the m-IBM performs the best for the whole range of isotopes from $N = 84$ to $N = 94$. In this model, eight parameters are used, but without a fit to the experimental data. An angular momentum term is included for all nuclei except $N = 84$. Except for the lightest Gd isotopes, where the calculations overestimate the experimental data, a reasonable agreement is obtained. The reason for these discrepancies is either a too-restricted model space (only s, d, and f bosons are used), or because a restricted Hamiltonian was used. We recall that the Hamiltonian used in Ref. [36] is not the most general form, but was adopted to match the one used in previous phenomenological calculations. Finally, the TPSM reproduces the experimental data in ^{150}Gd very well; the deviation is below 100 keV up to 10^+. Although not the main purpose of this paper, we note that the TPSM also reproduces the staggering of the excited levels in the γ band for deformed nuclei in the Nd-Dy region [16]. In addition, the TPSM is the only one among the five theoretical models employed in the present paper that includes the triaxial degrees of freedom. In the updated TPSM calculations of ^{150}Gd in this paper, the model predicts the axial quadrupole deformation of $\beta_2 = 0.284$ and the asymmetry parameter, $\gamma = 20.3^\circ$. This places ^{150}Gd in the rather deformed region, having also a considerable triaxiality which is responsible for the good reproduction of the experimental data. Although outside of the scope of the present investigation, it would be interesting to extend these calculations to the whole isotopic chain and benchmark the extent of the triaxial region in the rare-earth nuclei against the Monte Carlo shell-model calculations [5,6].

Out of all the theoretical models presented before, the QRPA (orange) and RQRPA (violet), TDHF (cyan), QOCH (red) [38], m-IBM (light green) [36], TPSM (dark green) [16], and the CQOM (blue) [40] are able to calculate both positive- and negative-parity states. Their results for the negative-parity states are presented on the right panels of Fig. 7 for odd spins between $J^\pi = 1^-$ and $J^\pi = 9^-$. QRPA, RQRPA, and TDHF calculations are only shown for the $J^\pi = 3^-$ states. Usually, the presence of the negative-parity states in the low-lying spectra of even-even nuclei is associated with octupole collectivity. Experimentally, an alternating parity sequence is observed for ^{148}Gd and ^{150}Gd to start already with the 2^+_1 and 3^-_1 states. For heavier isotopes, the octupole states are located at higher excitation energies, and except for the 3^-_1 levels, which have a rather constant trend, they present a decreasing energy down to $N = 90$–92, and remain constant for higher N values. Theoretical calculations predict the presence of such states at low energies. As in the case of the positive-parity states, the TPSM gives the best overall reproduction of experimental data across the spin range considered here. QRPA

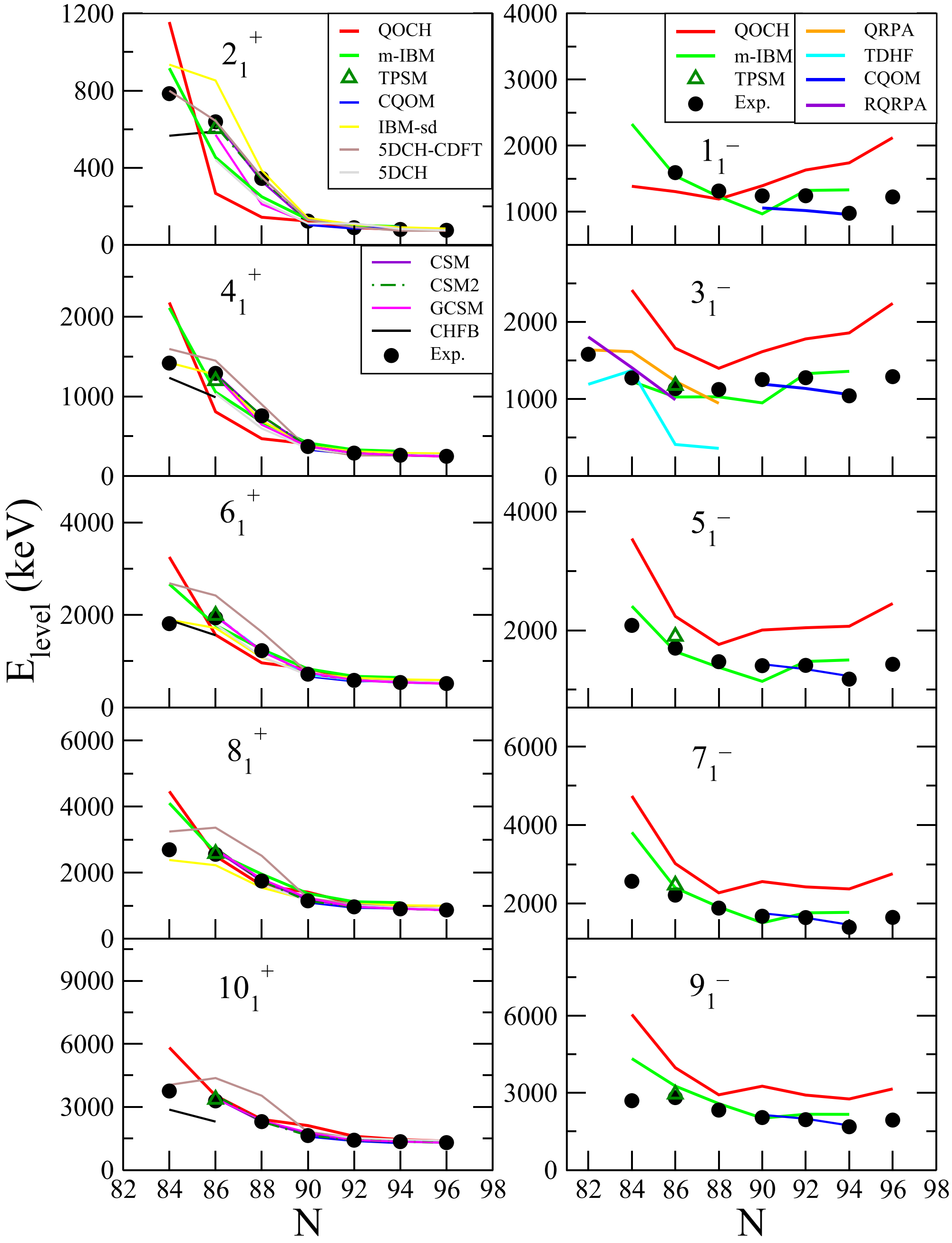

FIG. 7. Systematics of experimental (left) positive-parity and (right) negative-parity states in the yrast band of ^{146}Gd – ^{160}Gd in comparison with predictions of various theoretical models (solid lines): QOCH (red), mapped IBM (light green), TPSM (dark green triangle), QRPA (orange), RQRPA (violet, only the 3^- states), TDHF (cyan), CQOM (blue) [40], IBM-sd (yellow) [92], 5DCH-CDFT (brown) [15], 5DCH (grey) [20], CSM (violet, only positive-parity states), CSM2 (dark green dash-dotted line), GCSM (magenta) [93], and CHFB (black) [94].

and RQRPA models predict a decreasing trend of excitation energy for the 3_1^- states with decreasing neutron number, in good agreement with the experimental data. The TDHF calculations mark a sharp drop of the 3_1^- state energies at $N = 86$ (^{150}Gd), and a similar underestimated experimental value is also seen in the case of ^{152}Gd. In the m-IBM, with the exception of $N = 84$, the main trend is reproduced for all the Gd isotopes in this study. The presence of a minimum at $N = 90$ for all negative-parity states is explained by the disappearance of the octupole minimum in the mean-field PES starting with ^{154}Gd, where quadrupole deformation starts to dominate. The QOCH states are produced in general at much higher excitation energy than the experimental values due to a too small moment of inertia, as well as not including triaxial degrees of freedom. The CQOM calculations have only been performed for three isotopes, from ^{154}Gd to ^{158}Gd ($90 \leqslant N \leqslant 94$), but the reproduction of the experimental data is very good, especially for high angular momenta. It would

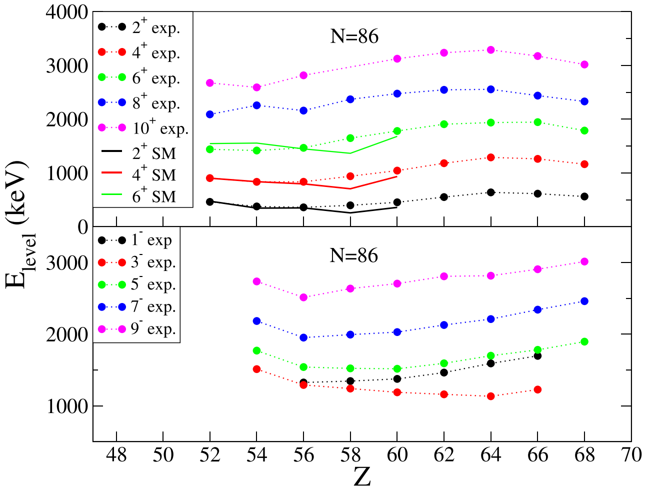

FIG. 8. Systematic of experimental (solid circles) positive- (upper panel) and negative-parity states (lower panel) in the yrast band of the $N = 86$ isotones in comparison with the predictions of the shell model (solid lines) [102].

be interesting to extend these calculations for other lighter isotopes ($N \leqslant 90$).

We present in Fig. 8 the systematic behavior of the excitation energies, both positive and negative parity, for the $N = 86$ isotones. Experimental data (circles) are taken from Refs. [33,88,96–101], while the theoretical calculations (solid lines) are those from Ref. [102] within the shell-model framework with the N3LOP interaction (only positive-parity states have been reported in Ref. [102]). The theoretical values are extracted from Figs. 1–5 of Ref. [102]. $N = 86$ nuclei have energy ratios $E_{4_1^+}/E_{2_1^+}$ of between 2.0 and 2.5, characteristic of transitional nuclei. The shell-model calculations support the presence of enhanced quadrupole correlations, as will be shown later in the case of transition strengths. Although not included in this plot, it is worth mentioning that the model supports the presence of triaxiality, with $\gamma \approx 10^\circ$ [102].

The evolution of the experimental 3_1^- state for the $N = 86$ isotones indicates that a minimum value is reached in the case of Gd ($Z = 64$), implying that the octupole correlations are stronger in the case of ^{150}Gd as compared to the other nuclei in the region. This should be reflected in the $B(E3)$ strength distribution.

2. Transition strengths

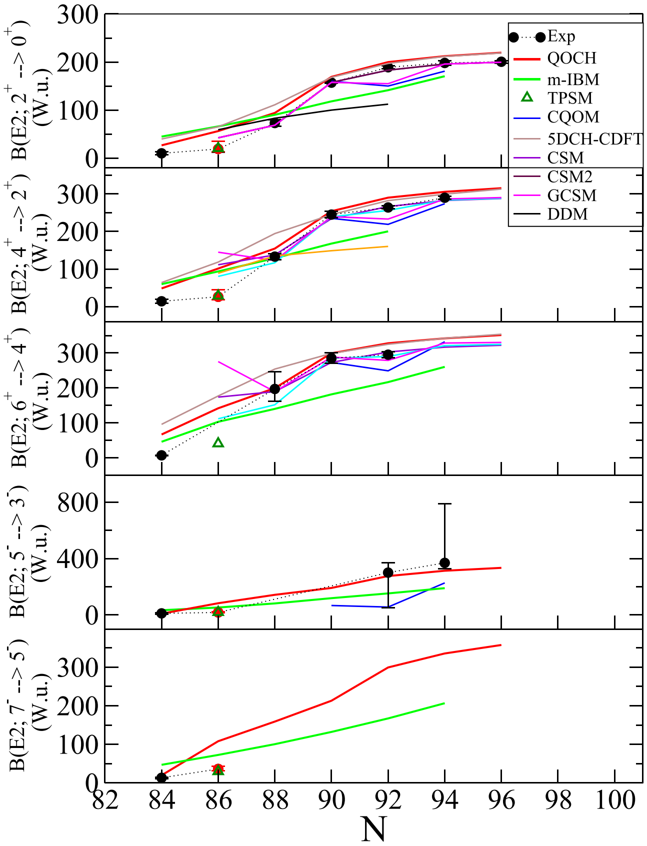

FIG. 9. Systematic of experimental $B(E2)$ transition probabilities in W.u. (solid black circles for the literature values, solid red circles for the values from the present work) in the yrast band and of the lowest-lying negative-parity band of the Gd isotopes in comparison with the predictions of different models (solid lines): QOCH (red) [38], mapped IBM (light green) [36], TPSM (dark green triangle) [16], CQOM (blue) [40], 5DCH-CDFT (brown) [15], CSM (violet), CSM2 (maroon), GCSM (magenta) [93], and DDM (black) [103].

The behavior of the $B(E2)$ transition strengths in the yrast band of Gd nuclei is examined in Fig. 9. We present the experimental data (solid circles, taken from the adopted levels of ENSDF [33,87–91]) in comparison with the theoretical values from the present calculations or from the literature (solid lines), when they were given in their respective papers: QOCH (red), m-IBM (light green), TPSM (dark green triangle), CQOM (blue) [40], 5DCH-CDFT (brown) [15], CSM (violet), CSM2 (maroon), GCSM (magenta) [93], and dynamic deformation model (DDM, black) [103]. In the case of ^{150}Gd, the best agreement with the experimental data is produced by the TPSM, most of the time having values within the experimental uncertainty. This implies that the essential degrees of freedom are captured for the $E2$ transition strengths, and it will be desired in the future to measure and compare the corresponding values in the γ band with these predictions. Among the other two different approaches, an overall better systematic reproduction of experimental data is found for the QOCH. Although this model predicts the negative-parity states at much higher excitation energies than observed experimentally (see Fig. 7), the quadrupole strength is fairly well reproduced, not only between the positive-parity states, but also between the negative-parity levels. An exception is the $7^- \rightarrow 5^-$ transition in ^{150}Gd ($N = 86$), which is overestimated. The m-IBM produces a flatter behavior than observed in the experiments for the positive-parity states, but gives a reasonable reproduction of the $E2$ strength of the negative-parity states. There are two models, the m-IBM and the DDM, which produce such a flat behavior for the $E2$ strength, implying that the shape/phase transition at $N = 90$ is not reproduced.

Experimental (solid circles) $E1$ ($3_1^- \rightarrow 2_1^+$, $4_1^+ \rightarrow 3_1^-$, $5_1^- \rightarrow 4_1^+$, $7_1^- \rightarrow 6_1^+$, and $8_1^+ \rightarrow 7_1^-$) and $E3$ ($3_1^- \rightarrow 0_1^+$) transition strengths are compared in Fig. 10 to the theoretical

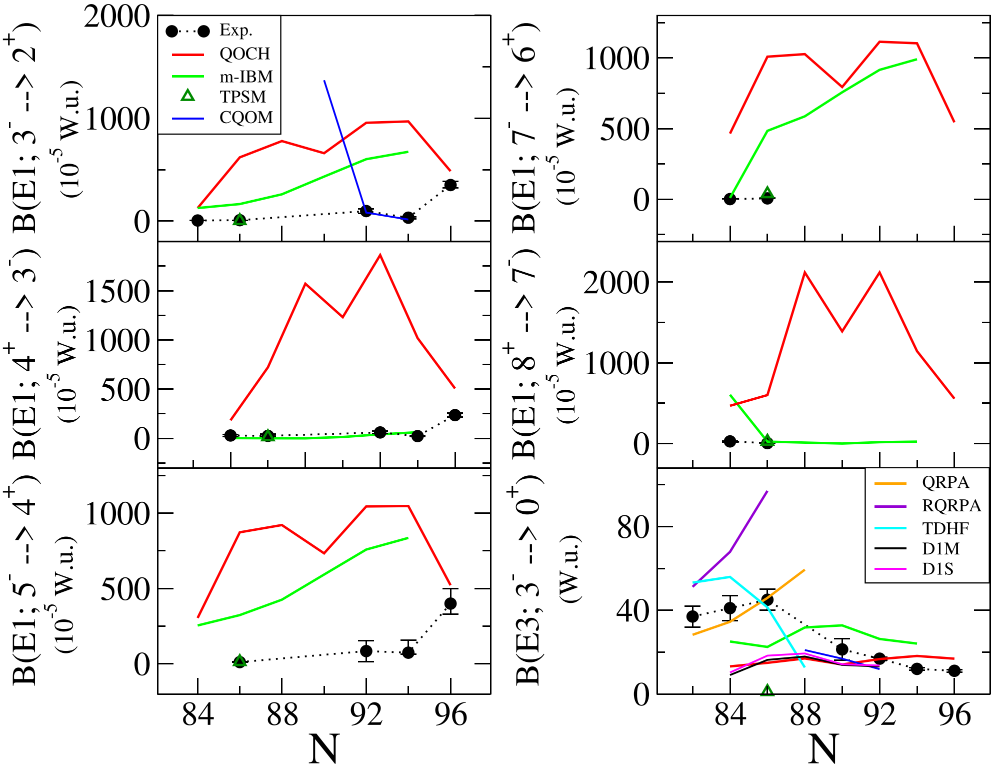

FIG. 10. Systematic of experimental $B(E1)$ and $B(E3)$ transition probabilities in 10^{-5} W.u. and W.u., respectively (solid circles) in the yrast band of the Gd isotopes in comparison with the predictions of different models (solid lines): QRPA (orange) and RQRPA (violet), TDHF (cyan), QOCH (red) [38], m-IBM (light green) [36], TPSM (dark green triangle) [16], CQOM (blue) [40], and D1M (black) and D1S (magenta) [39].

calculations (solid lines) within the QRPA (orange), RQRPA (violet), TDHF (cyan), QOCH (red) [38], m-IBM (light green) [36], TPSM (dark green triangle) [16], and CQOM (blue) [40] models. In addition, in the case of $E3$ transitions, the results from Ref. [39] are included as obtained from a mean-field calculation with the Gogny energy density functional using the D1M (black) and D1S (magenta) parametrizations. For the $E1$ transitions, the only theoretical model able to reproduce the experimental data in ^{150}Gd is the TPSM. With such a good agreement, one would expect the octupole degrees of freedom are completely captured by this model. However, the calculated $E3$ strength is too low, with only 1.1 W.u. This highlights the importance of measuring these values as a thorough test of theoretical predictions. The other models are having problems reproducing all the transition strengths, with most of the experimental data being overestimated by factors up to 100. The CQOM gives a good reproduction of the $3^-_1 \rightarrow 2^+_1$ strength in ^{156}Gd ($N = 92$) and ^{158}Gd ($N = 94$), but it predicts a value of about 10^{-2} W.u. for ^{154}Gd ($N = 90$), which although not yet measured experimentally, is about two orders of magnitude higher than the corresponding values in this region. The QOCH and the m-IBM models also predict similar values in the 10^{-2}–10^{-3} W.u. range.

For the $E3$ transitions, the best agreement with the experimental values is obtained for the QRPA calculations. The increasing trend predicted towards $N = 88$ is in full agreement with the result from the current work. An even higher value for ^{152}Gd is predicted (59 W.u.) by these spherical QRPA calculations, which still needs to be confirmed experimentally. Such a value was extracted for ^{152}Gd from inelastic scattering experiments [35] (52(17) W.u.), but this procedure is model dependent, and, as such, the experimental value was not included in Fig. 10. A similar increasing trend is also calculated by the RQRPA model, but the absolute values are much higher than the experimental values.

In Refs. [104,105], an interesting analysis of the components contributing to the $3^- \rightarrow 0^+$ transition strength has been performed in the case of ^{148}Gd. The authors have identified the main contribution of the $B(E3)$ value as arising from the $\nu i_{13/2} \rightarrow \nu f_{7/2}$ single-particle $E3$ transition. In our QRPA calculations using the SkX interaction, the first 3^- state in Gd nuclei is primarily formed by the proton $2d_{5/2}^{-1}1h_{11/2}$ excitation (63.62% for ^{150}Gd), followed by other proton transitions, such as $1g_{9/2}^{-1}1h_{11/2}$ and $1g_{7/2}^{-1}1h_{11/2}$, with relatively small contributions. As the neutron number increases from ^{146}Gd to ^{152}Gd, the energy of the first 3^- state decreases, and the $B(E3)$ strength increases, as expected. The neutron $2f_{7/2}^{-1}1i_{13/2}$ excitation also starts to play a role in the first 3^- state, although its contribution is suppressed due to a large energy difference between the states. Meanwhile, the contributions from proton transitions increase as they remain energetically more favorable, and their coherent contribution leads to an increase in the total $B(E3)$ strength. Similar results are obtained using the RQRPA with the DD-PCX interaction.

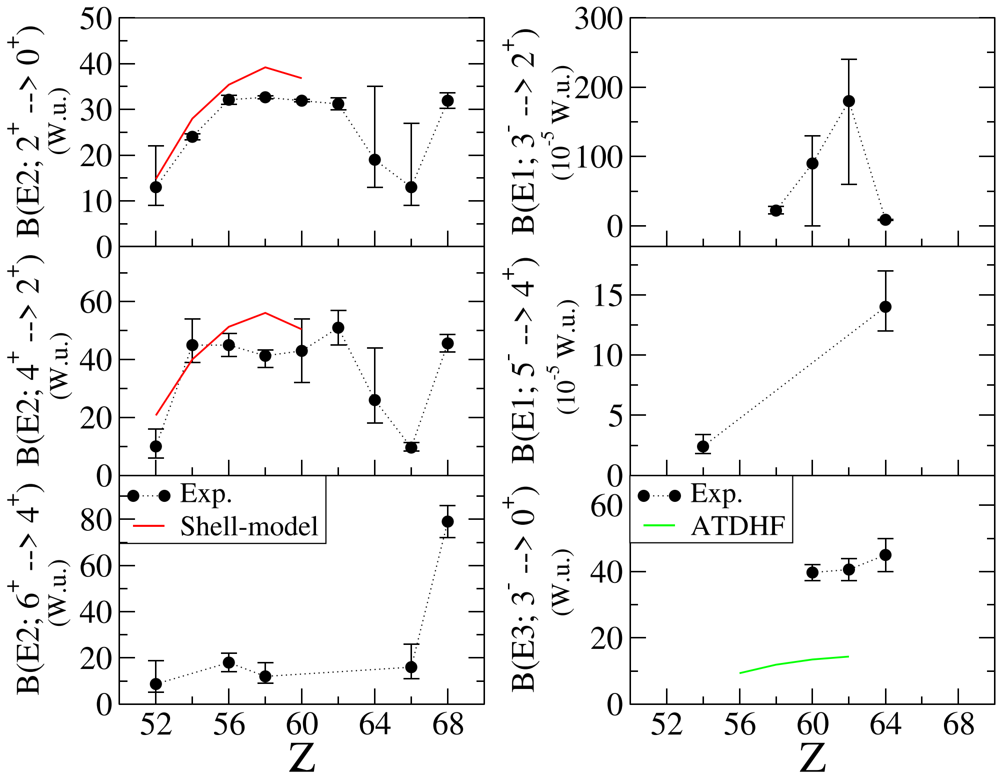

FIG. 11. Systematic of experimental transition probabilities ($E1$, $E2$, and $E3$) (solid circles) in the $N = 86$ isotones in comparison with the predictions of different models (solid lines): shell model [102] (red), ATDHF [42] (green). $E1$ transitions are given in 10^{-5} W.u. units, while the others are in W.u.

TDHF is the only model that predicts a maximum octupole collectivity in this region. However, this is located at $N = 84$, slightly shifted compared to the experimental trend. The value for ^{152}Gd ($N = 88$) is considerably lower than the ones for lighter Gd isotopes, marking an abrupt change in the population of single-particle states. A relatively constant behavior is predicted by all the other models in the case of the $E3$ $3_1^- \rightarrow 0_1^+$ transition strengths across the Gd isotopic chain, in contrast to the experimental situation.

Extended QRPA calculations for the Nd, Sm, Gd, and Dy isotopic chains in the $N = 82$–86 region, where the spherical assumption implied by the model is still valid, were presented in Ref. [34]. We remind the reader that these calculations indicated an increasing trend of the $B(E3)$ values with increasing Z, in addition to a saturation of these values towards Dy isotopes. More extensive QRPA calculations performed only for the $N = 82$ chain in this region indicate that a maximum octupole collectivity is found for ^{148}Dy. The different contributions of the $2d_{5/2} \rightarrow 1h_{11/2}$ proton configuration is seen in our calculations to be responsible for this behavior.

At the moment, the $B(E3)$ value of 45(5) W.u. for the $3^- \rightarrow 0^+$ transition strength in ^{150}Gd, obtained in Ref. [34] and the present work, is the highest and the most precise octupole strength measured in the rare-earth region according to the compilation of Kibedi and Spear [35]. As noted in Ref. [34] the maximum octupole collectivity in Sm and Nd isotopic chains is also obtained at $N = 86$. In addition, the $E3$ strength obtained for ^{150}Gd (45(5) W.u.) is close to the values obtained in the case of quadrupole-deformed ^{144}Ba (48^{+25}_{-34} W.u.) [2] and ^{146}Ba (48^{+21}_{-29} W.u.) [25], where the strongest octupole transitions in the rare-earth region are found so far.

In the present experiment, a value of 53^{+15}_{-12} W.u. was obtained for the $5_1^- \rightarrow 2_1^+ E3$ transition. The three models analyzed in this paper produce lower values than the experimental ones: 25.3 W.u. in QOCH, 28 W.u. in m-IBM, and 2.4 W.u. in TPSM. This emphasizes one more time that the models are having problems reproducing the $E3$ strengths.

The transition strengths of the $N = 86$ isotones are summarized in Fig. 11 for nuclei in the $Z = 52$ (Te) and $Z = 68$ (Er) range. Experimental data are presented with solid circles and are taken from Refs. [33,96,98–101,106,107], while the theoretical models used are the shell model (SM) from Ref. [102] for the $2_1^+ \rightarrow 0_1^+$ and $4_1^+ \rightarrow 2_1^+$ transitions, and the adiabatic time-dependent Hartree-Fock plus zero point energy in the cranking approximation (ATDHF) for the $3_1^- \rightarrow 0_1^+$ transition [42]. The $2_1^+ \rightarrow 0_1^+$ $E2$ transition strength shows an increase up to Ba nuclei ($Z = 56$), while a relatively constant behavior is displayed for heavier nuclei up to Er ($Z = 68$). The two notable exceptions are Gd ($Z = 64$) and Dy ($Z = 66$), but they have a large uncertainty and need to be measured more precisely. The shell model reproduces the increasing trend of collectivity, saturating around $Z = 56$, and comes quite close to reproducing the absolute values too. In addition, as mentioned previously, it predicts an increased triaxiality in the case of ^{140}Xe ($Z = 54$), ^{144}Ce ($Z = 58$), and ^{146}Nd ($Z = 60$), having γ values of 10°, 6°, and 8°, respectively. It would be interesting to expand these calculations to heavier nuclei, although there are considerable computational challenges. A similar trend is observed for the $4_1^+ \rightarrow 2_1^+$ transition, but while the value for Gd ($Z = 64$) obtained in the present paper has a large uncertainty and can still be regarded as in line with the other values, the one in Dy ($Z = 66$) has a small uncertainty with a very low value of only $9.6^{+1.8}_{-1.2}$ W.u. [96], which is surprising for a nucleus with the proton number in the middle of the $Z = 50$–82 shell. The $B(E2)$ strength is obtained from a recoil-distance lifetime measurement performed from singles spectra and reported only as an annual report in Ref. [108]. The authors knew at that time about the existence of the 60-ns isomeric state with $J^\pi = 17^+$ at 5088 keV, but they mention the results might be affected by the presence of another long-lived state between 3 and 5 MeV. Soon after, a new state with $J^\pi = 11^-$ at 3160.6 keV was found with a half-life of 4.3(9) ns [109] (revised to $J^\pi = 10^-$ and 3.9(9) ns [110]). The presence of this state very likely affects the mean lifetimes measured in singles in Ref. [108] and will need to be remeasured. The $6_1^+ \rightarrow 4_1^+$ strength has a relatively constant behavior with the exception of ^{154}Er [106], which would indicate the presence of an increased collectivity starting with Er nuclei. It would be interesting to measure the corresponding values in Yb ($Z = 68$) to follow the evolution of collectivity across the $N = 86$ isotonic chain.

Only a handful of experimental data on the $E1$ strength in the $N = 86$ nuclei exist. It is difficult to draw a conclusion based on these data points, which sometimes have quite large uncertainties. However, the experimental data support the presence of enhanced octupole correlations in the low-lying part of the $N = 86$ nuclei, with $E1$ strengths in the 10^{-3}–10^{-4} W.u. range. The $E3$ strengths known at this time have a constant behavior within their uncertainty limits, with values around 40 W.u., which supports the earlier claim of enhanced octupole correlations in these nuclei. The data are compared to the predictions of the adiabatic time-dependent Hartree-Fock plus zero point energy in the cranking approximation [42], and are lower than the experimental data by a factor of around 4. Nuclei heavier than $N = 86$ are better reproduced by this model. Clearly, more theoretical work is required.

3. Dipole moments

^{150}Gd nucleus, with $N = 86$, is located close to the octupole driving number at $N = 88$ and is therefore expected to show increased octupole correlations. The structure of ^{150}Gd presents alternating parity states starting as low as the 2^+ and 3^- states, which can be regarded as a signature for increased octupole collectivity. A better signature is the presence of enhanced $E1$ and $E3$ strengths, with $E1$ being usually easier to measure and for which more extensive data exist. In general, a $B(E1)$ value stronger than $\approx 10^{-5}$ W.u. is considered an indicator of reflection asymmetry [111].

In addition, increased $E1$ strength has been found in other $N = 86$ nuclei. For the $3_1^- \rightarrow 2_1^+$ transition, the highest $E1$ strength is found in ^{148}Sm, with a value of $1.8^{+6}_{-12} \times 10^{-3}$ W.u. However, this was surpassed in Ref. [26], which found in the case of ^{144}Ce that the $6_1^+ \rightarrow 5_1^-$ transition strength has the highest $E1$ strength in this region, with a value of $7.2^{+2.9}_{-1.9} \times 10^{-3}$ W.u., very close to the recommended upper limit of 0.01 W.u.

TABLE II. Experimental intrinsic dipole moments for ^{150}Gd (present paper) and ^{144}Ce [26] in comparison with the theoretical values from Ref. [112].

Nucleus	J^π	D_0^{expt} (e fm)	J^{th}	D_0^{th} (e fm)
^{150}Gd	3_1^-	0.041(3)		
	5_1^-	0.05(1)		
	7_1^-	0.03(1)		
	4_1^+	0.06(5)		
^{144}Ce	3_1^-	0.06(1)	0	0.17
	6_1^+	0.33(9)	5–9	0.20

More information can be gained by calculating the intrinsic dipole transition moment from the measured $B(E1)$ values. These values can be extracted using the rotational model formula given in Ref. [112]:

$$D_0^2 = \frac{4\pi}{3} B(E1) \frac{1}{\langle I_i 010 | I_f 0\rangle^2}, \tag{4}$$

where D_0 is the dipole moment, I_i and I_f are the initial and final angular momenta, and the $\langle I_i 010 | I_f 0\rangle$ is the Clebsch-Gordan coefficient. As pointed out in Ref. [112], although the nucleus we are applying the formula for is not a good rotor, it provides a unified way of extracting the dipole moments from the data across multiple regions. The extracted values for ^{150}Gd are presented in Table II, in comparison to the ones in ^{144}Ce, for which the theoretical values based on the reflection-asymmetric Woods-Saxon model from Ref. [112] are given too. The experimental dipole moments for the 3^- state in the two nuclei are similar and lower than the calculated dipole moment for the ground state in ^{144}Ce. This indicates once more that the octupole collectivity in this region is of vibrational character. The only value that is close to the theoretical predictions, and similar to the ones in much heavier Ra and Th nuclei, is the value for the 6^+ state in ^{144}Ce. This might indicate that the octupole deformation starts at higher spins. It would be very interesting to measure this $E1$ strength in the case of ^{150}Gd.

V. CONCLUSIONS

In summary, mean lifetimes in the $N = 86$ ^{150}Gd nucleus have been measured for the low-lying excited states using the recoil distance Doppler shift method, while complementary branching ratios have been extracted from an EC decay experiment. The newly deduced transition strengths fit well into the systematics of the neighboring isotopes and isotones. The deduced $B(E3; 3^- \rightarrow \text{g.s.})$ strength provides a direct evidence for increasing octupole collectivity in the Gd isotopic chain. The extracted $E1$, $E2$, and $E3$ transition strengths have been compared to the available models in the literature. In general, it is found that no theoretical model is able to reproduce the details of both the positive- and negative-parity states simultaneously. The QRPA and TDHF models come close to reproducing the $E3$ strength, but most of the other observables cannot be calculated yet within these models. The TPSM gives a fair reproduction of the experimental values but is unable to reproduce the $E3$ strengths. The m-IBM and QOCH calculations are in good agreement with the experimental values for the positive-parity states and the $E2$ transition strengths, but they considerably overestimate the $E1$ probabilities and predict a relatively constant behavior of the $E3$ strength, in contradiction with the expected peak around $N = 86$. Further experimental data are required to reduce the uncertainty of the 2_1^+ and 4_1^+ lifetimes and to measure the lifetime of the 6_1^+ state. On the theoretical side, more work is needed to understand the structure of this region, especially for the octupole degrees of freedom.

ACKNOWLEDGMENTS

We appreciate the excellent work of the Tandem accelerator team in delivering a high-intensity and stable beam throughout the two experiments. P.H.R. acknowledges support from the UK National Measurements System Programmes Unit of the UK's Department for Science, Innovation and Technology (DESIT). We are very grateful to R. Rodríguez-Guzmán for providing the $B(E3)$ values calculated within the D1S and D1M parametrizations of the Gogny interaction. This work is supported by the UK STFC under Grants No. ST/V001108/1 and No. ST/Y000358/1, and by the Romanian Nucleu Project No. PN 23 21 01 02. This project has received funding from the European Union's Horizon Europe Research and Innovation programme under Grant Agreement No. 101057511 (EURO-LABS).

---

[1] A. Bohr and B. R. Mottelson, *Nuclear Structure Vol. II* (Benjamin, New York, 1975).
[2] B. Bucher, S. Zhu, C. Y. Wu, R. V. F. Janssens, D. Cline, A. B. Hayes *et al.*, Phys. Rev. Lett. **116**, 112503 (2016).
[3] J. Dudek, D. Curien, I. Dedes, K. Mazurek, S. Tagami, Y. R. Shimizu, and T. Bhattacharjee, Phys. Rev. C **97**, 021302(R) (2018).
[4] K. Heyde and J. L. Wood, Rev. Mod. Phys. **83**, 1467 (2011).
[5] T. Otsuka, arXiv:2303.11299.
[6] T. Otsuka, Physics **4**, 258 (2022).
[7] F. Iachello, Phys. Rev. Lett. **87**, 052502 (2001).
[8] R. F. Casten and N. V. Zamfir, Phys. Rev. Lett. **87**, 052503 (2001).
[9] R. Krücken *et al.*, Phys. Rev. Lett. **88**, 232501 (2002).
[10] D. Tonev, A. Dewald, T. Klug, P. Petkov, J. Jolie, A. Fitzler, O. Möller, S. Heinze, P. von Brentano, and R. F. Casten, Phys. Rev. C **69**, 034334 (2004).
[11] Z.-Q. Sheng and J.-Y. Guo, Mod. Phys. Lett. A **20**, 2711 (2005).
[12] R. Fossion, D. Bonatsos, and G. A. Lalazissis, Phys. Rev. C **73**, 044310 (2006).
[13] L. K. Peker, J. H. Hamilton, and J. O. Rasmussen, Phys. Lett. B **110**, 99 (1982).
[14] K. Nomura and Y. Zhang, Phys. Rev. C **99**, 024324 (2019).
[15] Z. Shi, Q. B. Chen, and S. Q. Zhang, Eur. Phys. J. A **54**, 53 (2018).
[16] T. Naz, G. H. Bhat, S. Jehangir, S. Ahmad, and J. A. Sheikh, Nucl. Phys. A **979**, 1 (2018).
[17] S. Quan, Z. P. Li, D. Vretenar, and J. Meng, Phys. Rev. C **97**, 031301(R) (2018).
[18] S. Ebata and T. Nakatsukasa, Phys. Scr. **92**, 064005 (2017).
[19] R. Rodríguez-Guzmán and P. Sarriguren, Phys. Rev. C **76**, 064303 (2007).
[20] J. Libert, J.-P. Delaroche, M. Girod, H. Goutte, S. Hilaire, S. Péru, N. Pillet, and G. F. Bertsch, J. Phys.: Conf. Ser. **205**, 012007 (2010).
[21] E. A. McCutchan, N. V. Zamfir, and R. F. Casten, Phys. Rev. C **69**, 064306 (2004).
[22] G. A. Lalazissis, M. M. Sharma, and P. Ring, Nucl. Phys. A **597**, 35 (1996).
[23] T. R. Rodríguez and J. L. Egido, AIP Conf. Proc. **1090**, 419 (2009).
[24] P. A. Butler, Acta Phys. Pol. B **24**, 117 (1993).
[25] B. Bucher, S. Zhu, C. Y. Wu, R. V. F. Janssens, R. N. Bernard, L. M. Robledo *et al.*, Phys. Rev. Lett. **118**, 152504 (2017).
[26] M. Beckers *et al.*, Phys. Rev. C **102**, 014324 (2020).
[27] P. A. Butler, J. Phys. G: Nucl. Part. Phys. **43**, 073002 (2016).
[28] R. J. Keddy, Y. Yoshizawa, B. Elbek, B. Herskind, and M. C. Olesen, Nucl. Phys. A **113**, 676 (1968).
[29] P. A. Butler, Proc. R. Soc. A **476**, 20200202 (2020).
[30] P. E. Garrett *et al.*, Phys. Rev. Lett. **103**, 062501 (2009).
[31] P. Kleinheinz, M. Ogawa, R. Broda, P. J. Daly, D. Haenni, H. Beuscher, and A. Kleinrahm, Z. Phys. A **286**, 27 (1978).
[32] Zs. Podolyák, P. G. Bizzeti, A. M. Bizzeti-Sona, S. Lunardi, D. Bazzacco, A. Dewald, A. Algora, G. de Angelis, E. Farnea, A. Gadea, D. R. Kasemann *et al.*, Eur. Phys. J. A **17**, 29 (2003).
[33] S. K. Basu and A. A. Sonzogni, Nucl. Data Sheets **114**, 435 (2013).
[34] S. Pascu *et al.*, companion paper, Phys. Rev. Lett. **134**, 092501 (2025).
[35] T. Kibedi and R. H. Spear, At. Data Nucl. Data Tables **80**, 35 (2002).
[36] K. Nomura, R. Rodríguez-Guzmán, and L. M. Robledo, Phys. Rev. C **92**, 014312 (2015).
[37] W. Zhang, Z. P. Li, S. Q. Zhang, and J. Meng, Phys. Rev. C **81**, 034302 (2010).
[38] S. Y. Xia, H. Tao, Y. Lu, Z. P. Li, T. Nikšić, and D. Vretenar, Phys. Rev. C **96**, 054303 (2017).
[39] R. Rodríguez-Guzmán, L. M. Robledo, and P. Sarriguren, Phys. Rev. C **86**, 034336 (2012).
[40] N. Minkov, S. Drenska, M. Strecker, W. Scheid, and H. Lenske, Phys. Rev. C **85**, 034306 (2012).
[41] W. Urban *et al.*, Phys. Lett. B **258**, 293 (1991).
[42] J. L. Egido and L. M. Robledo, Nucl. Phys. A **545**, 589 (1992).
[43] D. Bucurescu *et al.*, Nucl. Instrum. Methods Phys. Res., Sect. A **837**, 1 (2016).
[44] A. Dewald, S. Harissopulos, and P. von Brentano, Z. Phys. A: At. Nucl. **334**, 163 (1989).
[45] G. Böhm, A. Dewald, P. Petkov, and P. von Brentano, Nucl. Instrum. Methods Phys. Res., Sect. A **329**, 248 (1993).
[46] A. Dewald, O. Möller, and P. Petkov, Prog. Part. Nucl. Phys. **67**, 786 (2012).

[47] B. Saha, computer code napatau (unpublished).

[48] T. Kibédi, Jr., T. W. Burrows, M. B. Trzhaskovskaya, P. M. Davidson, and C. W. Nestor, Jr., Nucl. Instrum. Methods Phys. Res., Sect. A **589**, 202 (2008).

[49] F. G. Kondev, Nucl. Data Sheets **109**, 1527 (2008).

[50] S. Pascu *et al.* (unpublished).

[51] W. D. Kulp *et al.*, Phys. Rev. C **76**, 034319 (2007).

[52] C. Baktash, E. der Mateosian, O. C. Kistner, A. W. Sunyar, D. Horn, and C. J. Lister, Contrib. Intern. Conference on Band Structure and Nuclear Dynamics, 146 (1980).

[53] C. Baktash, Proc. Conference on High Angular Momentum Properties of Nuclei, 207 (1983).

[54] D. R. Haenni and T. T. Sugihara, Phys. Rev. C **16**, 1129 (1977).

[55] E. der Mateosian and J. K. Tuli, Nucl. Data Sheets **75**, 827 (1995).

[56] E. der Mateosian, Nucl. Data Sheets **48**, 345 (1986).

[57] P. Ring and P. Schuck, *The Nuclear Many-Body Problem* (Springer, Berlin, 2004).

[58] N. Paar, P. Ring, T. Nikšić, and D. Vretenar, Phys. Rev. C **67**, 034312 (2003).

[59] N. Paar, D. Vretenar, E. Khan and G. Colò, Rep. Prog. Phys. **70**, R02 (2007).

[60] G. Colò, L. Cao, N. Van Giai, and L. Capelli, Comput. Phys. Commun. **184**, 142 (2013).

[61] E. Yüksel, G. Colò, E. Khan, and Y. F. Niu, Phys. Rev. C **97**, 064308 (2018).

[62] B. A. Brown, Phys. Rev. C **58**, 220 (1998).

[63] E. Yüksel, T. Marketin, and N. Paar, Phys. Rev. C **99**, 034318 (2019).

[64] C. Simenel, Eur. Phys. J. A **48**, 152 (2012).

[65] A. Bulgac and M. M. Forbes, *Energy Density Functional Methods for Atomic Nuclei* (IOP Publishing, Bristol, UK, 2019).

[66] Abhishek, P. Stevenson, Y. Shi, E. Yüksel, and A. S. Umar, Comput. Phys. Commun. **301**, 109239 (2024).

[67] J. Bartel, P. Quentin, M. Brack, C. Guet, and H.-B. Hakansson, Nucl. Phys. A **386**, 79 (1982).

[68] P. D. Stevenson and S. Fracasso, J. Phys. G: Nucl. Part. Phys. **37**, 064030 (2010).

[69] P. Marević, J.-P. Ebran, E. Khan, T. Nikšić, and D. Vretenar, Phys. Rev. C **97**, 024334 (2018).

[70] F. Iachello and A. Arima, *The Interacting Boson Model* (Cambridge University Press, Cambridge, UK, 1987).

[71] A. Arima and F. Iachello, Ann. Phys. **99**, 253 (1976).

[72] A. Arima and F. Iachello, Ann. Phys. **111**, 201 (1978).

[73] O. Scholten, F. Iachello, and A. Arima, Ann. Phys. **115**, 325 (1978).

[74] M. Babilon, N. V. Zamfir, D. Kusnezov, E. A. McCutchan, and A. Zilges, Phys. Rev. C **72**, 064302 (2005).

[75] P. von Brentano, N. V. Zamfir, and A. Zilges, Phys. Lett. B **278**, 221 (1992).

[76] N. Pietralla, P. von Brentano, and A. F. Lisetskiy, Prog. Part. Nucl. Phys. **60**, 225 (2008).

[77] K. Nomura, N. Shimizu, and T. Otsuka, Phys. Rev. Lett. **101**, 142501 (2008).

[78] J. Decharge, M. Girod, and D. Gogny, Phys. Lett. B **55**, 361 (1975).

[79] K. Hara and Y. Sun, Int. J. Mod. Phys. E **04**, 637 (1995).

[80] K. Hara and S. Iwasaki, Nucl. Phys. A **332**, 61 (1979).

[81] K. Hara, S. Iwasaki, and K. Tanabe, Nucl. Phys. A **332**, 69 (1979).

[82] K. Hara and S. Iwasaki, Nucl. Phys. A **348**, 200 (1980).

[83] J. A. Sheikh and K. Hara, Phys. Rev. Lett. **82**, 3968 (1999).

[84] J. A. Sheikh, G. H. Bhat, W. A. Dar, S. Jehangir, and P. G. Ganai, Phys. Scr. **91**, 063015 (2016).

[85] S. Jehangir, G. H. Bhat, J. A. Sheikh, R. Palit, and P. A. Ganai, Nucl. Phys. A **968**, 48 (2017).

[86] Y. Sun, K. Hara, J. A. Sheikh, J. G. Hirsch, V. Velázquez, and M. Guidry, Phys. Rev. C **61**, 064323 (2000).

[87] N. Nica, Nucl. Data Sheets **117**, 1 (2014).

[88] C. W. Reich, Nucl. Data Sheets **110**, 2257 (2009).

[89] C. W. Reich, Nucl. Data Sheets **113**, 2537 (2012).

[90] N. Nica, Nucl. Data Sheets **141**, 1 (2017).

[91] N. Nica, Nucl. Data Sheets **176**, 1 (2021).

[92] J. E. García-Ramos, J. M. Arias, J. Barea, and A. Frank, Phys. Rev. C **68**, 024307 (2003).

[93] A. A. Raduta and A. Faessler, J. Phys. G: Nucl. Part. Phys. **31**, 873 (2005).

[94] R. N. Majumdar, Phys. Rev. C **61**, 064312 (2000).

[95] https://apps.automeris.io/wpd/

[96] M. J. Martin, Nucl. Data Sheets **114**, 1497 (2013).

[97] J. Chen, Nucl. Data Sheets **146**, 1 (2017).

[98] N. Nica, Nucl. Data Sheets **154**, 1 (2018).

[99] T. D. Johnson, D. Symochko, M. Fadil, and J. K. Tuli, Nucl. Data Sheets **112**, 1949 (2011).

[100] A. A. Sonzogni, Nucl. Data Sheets **93**, 599 (2001).

[101] Yu. Khazov, A. Rodionov, and G. Shulyak, Nucl. Data Sheets **136**, 163 (2016).

[102] H. Naïdja, F. Nowacki, and B. Bounthong, Phys. Rev. C **96**, 034312 (2017).

[103] H. Tagziria, W. D. Hamilton, and K. Kumar, J. Phys. G: Nucl. Part. Phys. **16**, 1837 (1990).

[104] G. de Angelis, P. Kleinheinz, B. Rubio, J. L. Tain, K. Zuber, B. Brinkmöller, P. von Rossen, J. Römer, D. Paul, J. Meißburger, G. P. A. Berg, A. Magiera, G. Hlawatsch, L. G. Mann, T. N. Massey, D. Decman, G. L. Struble, and J. Blomqvist, Z. Phys. A **336**, 375 (1990).

[105] M. Piiparinen, P. Kleinheinz, S. Lunardi, M. Ogawa, G. de Angelis, F. Soramel, W. Meczynski, and J. Blomqvist, Z. Phys. A **337**, 387 (1990).

[106] A. E. Turturica *et al.*, Phys. Rev. C (2025) (to be published).

[107] G. Häfner *et al.*, Phys. Rev. C **103**, 034317 (2021).

[108] E. H. du Marchie van Voorthuysen, W. Moonen, J. F. W. Jansen, and M. J. A. de Voigt, KVI Ann. Rep. **1978**, 63 (1979).

[109] Y. Nagai, J. Styczen, M. Piiparinen, and P. Kleinheinz, Z. Phys. A **296**, 91 (1980).

[110] J. Styczen, Y. Nagai, M. Piiparinen, A. Ercan, and P. Kleinheinz, Phys. Rev. Lett. **50**, 1752 (1983).

[111] P. A. Butler and W. Nazarewicz, Rev. Mod. Phys. **68**, 349 (1996).

[112] P. A. Butler and W. Nazarewicz, Nucl. Phys. A **533**, 249 (1991).